Final Technical Report

Evolution of Permeability and Strength Recovery of Shear Fracture Under Hydrothermal Conditions

Award Recipient Organization: University of Utah (DOE Project DE-EE0007080)

Subrecipient Organization:
U.S. Geological Survey
DUNS Identifier: 074672841
350 N Akron Rd, Moffett Field, CA, 94035
Award Number: 5-2565

Project Period:
10/01/2021 – 12/31/2024

Principal Investigator:
David Lockner
Research geophysicist (Emeritus), USGS
dlockner@usgs.gov | 650-329-4826

Joshua Taron
Research geophysicist, USGS
jmtaron@usgs.gov | 650-439-2640

Tamara Jeppson
Research geophysicist, USGS
tjeppson@usgs.gov | 650-439-2559

Report Submitted By:
Tamara Jeppson
Date of Report Submission: 06/04/2025
Reporting Period: 10/01/2021 – 12/31/2024
Total Pages (excluding cover page): 46

Project Partners: None

This material is based upon work supported by the U.S. Department of Energy under Award Number DE-EE0007080.

Abstract

Final Report for Evolution of Permeability and Strength Recovery of Shear Fracture Under Hydrothermal Conditions

DOE Award Number:
Award Recipient Organization: University of Utah (DOE Project DE-EE0007080)
Subrecipient Organization: U.S. Geological Survey (Award Number: 5-2565)
Principal Investigator: David Lockner (Research geophysicist, Emeritus), Joshua Taron (Research geophysicist), Tamara Jeppson (Research geophysicist)

Geothermal energy is a clean and renewable resource that depends on the ability to move water through hot rock. In many locations, the ability to move water through rock requires the presence of extensive natural or human-made systems of fractures. However, these fracture systems are influenced by a variety of complex processes that occur at the temperature and pressure conditions found in geothermal reservoirs. To make geothermal systems more efficient, it is important to understand how the fractures evolve over time in response to these processes. This study explored how fractures in rock change under high-temperature and pressure conditions like those found in geothermal reservoirs, through laboratory experiments and numerical simulations. In general, fractures tend to close due to pressure from the surrounding rock preventing the flow of water. One set of laboratory experiments revealed that fractures in granitic rock can weaken over time at elevated temperatures, becoming more susceptible to slip. In many cases, fractures that slip become more permeable to fluid flow and can potentially sustain this permeability through changes in reservoir conditions. This study also showed that at the highest temperature examined (250 °C) large differences between the chemical composition of the rock and the fluid moving through it could improve water flow temporarily, likely due to the water dissolving parts of the rock. Flow rate predicted by models shows overall good agreement with the flow rate measured in our experiments but with some long time-scale variations that may be due to mechanical wear, or damage, of the fracture surface. A second set of experiments found that, over the temperature range examined, the closure of fractures was caused by brittle failure driven by high stresses at points where fracture surfaces were in contact. This result indicates that fracture closure in geothermal reservoirs could be counteracted by maintaining high pore pressures. Additionally, we also tested a new method using electrical resistance to measure fracture closure in controlled systems with high precision.

Keywords: Enhanced Geothermal Systems, Fluid-Rock Interactions, THMC Processes, Fracture Evolution

Table of Contents

Final Report for Evolution of Permeability and Strength Recovery of Shear Fracture Under Hydrothermal Conditions

Principal Investigator: Tamara Jeppson, Research geophysicist; Joshua Taron, Research geophysicist; David Lockner, Research geophysicist

1 Executive Summary

1.1 Background

Economical geothermal reservoir operations rely on the presence of long-lived, large-volume and high-heat-transfer-area permeable fracture systems. The ability to create and/or reactivate and subsequently sustain these systems is strongly influenced by complexly coupled mechanical (M) and chemical (C) processes in reservoirs forced from equilibrium by hydraulic stimulation (H) and thermal drawdown (T). Understanding feedbacks among these strongly coupled THMC processes (Taron et al., 2016) as they relate to fracture permeability and strength is of first-order importance in the design of Enhanced Geothermal Systems (EGS).

Fractures and faults respond to THMC interactions at a variety of strengths and spatial and temporal scales. While hydraulic and thermal stimulation has been generally effective at generating permeability and surface area within EGS reservoirs, the magnitude of the response to stimulation and its persistence over sustained periods of thermal and chemical disequilibrium remain poorly understood. This uncertainty relates not only to the style of reservoir modeling, but to the fact that process interactions within fractures are poorly understood.

Experimental data regarding the evolution of fractures at geothermal conditions are sparse, particularly during the process of shear. Most laboratory studies have tended to focus on how fracture permeability evolves at elevated temperatures in stationary fractures (e.g., Polak et al., 2003) or on how fracture permeability evolves with shear at room temperature (e.g., Im et al., 2019). A few modeling studies have attempted to replicate observed fracture behavior at elevated temperature (e.g., Taron & Elsworth, 2010) and healing alongside shear at reservoir scale (e.g., Taron et al., 2016). Relatively little has been done to examine the complex interplay among mechanisms, processes, and resulting changes in fracture properties. In our study we investigated the evolution of fracture properties at elevated temperatures by integrating laboratory and modeling efforts.

1.2 Objectives

The primary goal of our project was to determine how THMC processes affect the sustainability of fracture networks in geothermal reservoirs and provide strategies for improving EGS techniques that maximize thermal coupling and increase reservoir longevity. To do this we integrated laboratory data and numerical models to constrain and define micromechanical models for the temporal evolution of the properties of shear and static fractures (e.g., permeability and compliance) as a function of temperature and pressure. Our main technical objectives were:

- Qualify and quantify rates of change of fracture properties

- Parameterize modes of reaction
- Develop micromechanical and empirical fracture models
- Extend THMC models for laboratory- and reservoir-scale application.

1.3 Key Findings

Our triaxial shear experiments were focused on understanding how THMC process will influence the evolution of strength and permeability in fracture network in geothermal reservoirs. We observed decreases in fracture strength with time at elevated temperatures, this promotes aseismic creep which may help to keep fractures in geothermal reservoirs open and limit sealing. The underlying mechanism is still to be determined but it clearly depends on the presence of liquid-phase water, is temperature-dependent and chemically complex. Our preliminary results indicate the observed weakening may be due to precipitation of weak secondary minerals. The crack hydraulic transmissivity data acquired during these triaxial experiments suggests permeability could be enhanced by stimulating the reservoir using fluid that is undersaturated with respect to the rock composition. This would drive the system from equilibrium promoting dissolution which may help to enhance transmissivity at elevated temperatures. However, this effect may be short lived as dissolution of surface contacts would eventually lead to fracture closure.

Simulated single fracture convergence tests were designed to examine the evolution of hydraulically-generated, opening-mode fractures through direct measurement of closure and aperture as a function of time, effective stress, temperature and initial aperture.
These tests revealed significant closure, primarily driven by brittle failure under stress rather than ductile deformation. These results indicate that closure could be reduced and reservoir longevity increased by maintaining high pore pressure in the reservoir. This would reduce the stress at asperities thereby reducing brittle failure and sustaining permeability. Quartz mobility was found to be slow at reservoir conditions, minimizing concerns about permeability reduction due to mineral deposition. The electrical resistance measurements effectively tracked fracture closure with high precision. This provides a method to determine closure in real time in controlled experiments, providing data on when and why closure is occurring.

Experimental data provided rate constants and validation for numerical models that can be used to help with reservoir planning. Our creep model predictions show reasonable agreement with the rates of healing and magnitudes of dilation observed in triaxial experiments. At larger timescales across all stages of slip, there is a background exponential decay that is not predicted by the creep model. This long-term rate of healing reduces the expected dilation and/or occludes flow paths. This difference between predicted and observed decay could be due to wear of the surface although it may have other origins. It is unlikely to be caused by a bulk mineral-precipitation effect given the net dissolution environment with undersaturated influent. We find that a two-stage empirical model reliably captures the observed experimental behavior and there is a strong adherence of healing rate to the two-stage degradation across all stages of slip.

2 Introduction

2.1 Purpose of the Report

There is growing interest in geothermal energy due to its potential as a renewable, reliable, and low-emission energy source that can be used to supplement intermittent renewable energy sources such as solar or wind. The Frontier Observatory for Research in Geothermal Energy (Utah FORGE) is an underground field-scale laboratory focused on the development and testing of EGS technologies. Effective EGS requires not just the ability to create a productive fracture network but also the ability to maintain that productivity of that system over an extended period. Reservoir planning requires an understanding of how fluid-rock interactions and fracture properties will influence reservoir behavior over time. To assist with this, our project sought to integrate experimental studies with THMC modeling to determine fracture behavior and permeability evolution over time at conditions consistent with the Utah FORGE reservoir (~200 °C, ~40 MPa effective vertical stress at 10950 ft MD). This report summarizes the results of those experiments and numerical models. It is the final report for work performed under award 5-2565, submitted in accordance with the closeout procedure.

2.2 Scope of Work

This study employed a combination of laboratory experiments and numerical modeling to quantify changes in fracture properties over time, develop micromechanical and empirical models, and assess the impact of THMC mechanisms at both laboratory and reservoir scales. The research focused on understanding how THMC processes influence fracture networks in EGS. The primary tasks included laboratory-based triaxial shear and single-fracture convergence tests under controlled hydrothermal conditions to measure permeability evolution and fracture healing. The experimental work was followed by data analysis and model development to refine tools for EGS.

The project milestones included (1) development of operational experimental setups, (2) completion of laboratory tests to determine rates of evolution of fracture properties, (3) refinement of micromechanical models, (4) validation of THMC numerical simulators, and (5) dissemination of findings through conference presentations and peer-reviewed publications. Key deliverables included experimental datasets characterizing fracture permeability and strength evolution, high-resolution 3D surface profiles, and numerical simulations for laboratory and reservoir-scale modeling of fracture evolution in response to THMC processes.

2.3 Organization of the Report

In this report we first present the experimental and computation methods used in this study. We then present the results of our work and implications of our results for Utah FORGE and EGS technologies. We include a discussion of the limitations of the current study and lessons learned. Finally, the conclusions of the project are summarized and potential avenues for future exploration are presented.

3 Methodology

3.1 Triaxial shear experiments

Laboratory slide-hold-slide (SHS) shear experiments were conducted in a conventional triaxial loading configuration. In these experiments, intervals of shearing on simulated fracture surfaces are separated by quasi-static hold periods (Fig. B1a). These experiments are normally focused on characterizing the time-dependent evolution of fracture strength, but in this study the experiments were combined with flow-through tests to examine the joint evolution of fracture strength and fluid transport properties.

The experiments were performed using cylindrical samples of Westerly granite and samples taken from Utah FORGE Well 16A(78)-32. Well 16A(78)-32 is an inclined borehole that was drilled to 10,897 ft measured depth (MD) (8,559 ft true vertical depth) with three coring runs from 5,473-5,505 ft MD; 5,846-5,892 ft MD; and 10,955-10,987 ft MD. The borehole functions as an injection well and was hydraulicly fractured at depths greater than 10,000 ft MD. The rock penetrated by the borehole is granitic. In this study we examined core samples from the last coring run. Sample UF7 was recovered from ~ 10957.8 ft MD and is a fine-grained, biotite-rich gneiss while sample UF10, recovered from ~10975.2 ft MD, is a quartz-rich granitoid. We performed preliminary X-ray diffraction and petrographic analysis of these samples which indicated UF10 is composed of plagioclase, K-feldspar, quartz, and muscovite while the composition of UF7 is plagioclase, quartz, and biotite. Westerly granite is primarily composed of plagioclase, K-feldspar, quartz, and biotite. We examined two different sample geometries: smooth and rough fractures.

3.1.1 Smooth fractures

Smooth fracture experiments were conducted using cylindrical samples (25.4 mm diameter, ~ 61 mm length) that were cut at a 30° angle relative to the sample axis. The cut surfaces were ground flat and roughened with #240 grit sandpaper to attain relatively reproduceable surfaces with RMS height of ~ 10 µm. Shearing of these roughened surfaces results in the development of a very thin layer of ultrafine gouge particles. Offset boreholes (2.38 mm diameter) were drilled into each sample half to provide fluid access to the simulated fault surface (Fig. B1b) and a groove was scribed into the sawcut surface, intersecting the boreholes perpendicular to the long axis of the surface, to help distribute the pore fluid and facilitate near-parallel flow between the boreholes.

3.1.2 Rough fractures

Only Westerly granite was used in the experiments on the rough-fracture geometry. A cylindrical sample (22 mm diameter, ~61 mm length) was notched to promote failure along a plane inclined at a 30 ° angle relative to the sample axis. Offset boreholes were drilled into the top and bottom of the sample to intersect this same plane. The notches were then filled with rounded quartz gouge and the sample was inserted into a latex jacket. The jacketed sample was then placed in the pressure vessel and a constant confining pressure of 20 MPa was applied. The sample was axially loaded at a rate of 0.5 μm/s until it failed, generating a realistically rough fracture with RMS height on the order of 100 to 1000 µm-scale roughness (Fig. B2).

After failure, the sample was removed from the pressure vessel and inspected to verify that the resulting fracture intersected the pre-drilled boreholes. Gouge generated by sample failure was removed and the fracture surfaces were scanned with a 3D optical profilometer. Afterwards the sample halves were reassembled, large gaps along the perimeter of the fracture were filled with rounded quartz gouge, and the sample was inserted into a Teflon jacket with a 1.7 mm wall thickness.

3.1.3 Experiment setup

The triaxial apparatus used in this study is internally heated and uses argon gas as the confining medium. Samples were isolated from the confining medium using lead tubes with 1.0 mm wall thickness (Fig. B1b). Double O-ring seals at both ends of the assembled samples prevent the argon gas from intruding into the sample. Experiments were conducted at temperatures from 22 to 250 °C, a constant confining pressure of 30 MPa (Westerly granite samples) or 50 MPa (Utah FORGE samples), and an average pore pressure of 10 MPa. Deionized water was used as the pore fluid. In our standard flow-through tests, a dual-piston syringe pump was used to apply a fixed pressure of 11 MPa at the top of the sample (inlet) and 9 MPa at the bottom of the sample (outlet), providing a 2 MPa pressure differential across the sample. Flow was always in the same direction and as fluid left the sample it was collected in a reservoir and periodically sampled for cation analysis. For comparison a suite of tests without flow-through were also conducted. In these no-flow tests, pore fluid was introduced to the system and allowed to equilibrate for 24 hours at the experiment temperature and pressure conditions before shearing was initiated. Pore pressure was held constant at 10 MPa.

After an initial run-in period where the sample experienced 0.9 mm of axial displacement, the sample was subjected to a sequence of alternating shearing intervals at shortening rate of 0.1 μm/s and quasi-static hold periods that ranged in duration from 100 to 500,000 s (~5.8 days). Flow rate data were collected continuously during both the shear and hold periods. The raw mechanical data were corrected for elastic deformation of the loading system, jacket strength, confining-pressure-dependent piston seal friction, and the reduction in contact area during deformation (refer to Tembe et al., 2010). At the conclusion of the experiment the samples were removed and the fracture surfaces scanned with a 3D optical profilometer. Gouge was removed from the rough surfaces prior to scanning but left on the smooth surfaces for later examination using a scanning electron microscope.

3.1.4 Quantifying strength evolution

In a standard sequence of SHS tests, when sliding resumes after a hold period a peak in the shear strength is observed (τ_{peak}) followed by a return to steady-state sliding friction (τ_{stable}) (Fig. B1a). The difference between the peak strength and the steady state friction measured before the hold is used to quantify the change in strength during the hold period ($\Delta\mu$). A time-dependent increase in fracture strength with the log of hold duration has been well documented in a variety of materials during SHS experiments at room temperature. However, our work shows that under geothermal conditions, granitic materials exhibit a transition to

time-dependent weakening (Jeppson et al., 2023). The observed evolution of frictional strength can be captured by the following relation:

$$\frac{\tau_{peak}}{\sigma_{N_{peak}}} - \frac{\tau_{stable}}{\sigma_{N_{stable}}} = \Delta\mu = \beta_1 \ln\left(\frac{t_h}{t_{c1}} + 1\right) + \beta_2 \ln\left(\frac{t_h}{t_{c2}} + 1\right) \quad [1]$$

where σ_{Npeak} and $\sigma_{Nstable}$ are the effective normal stress associated with the peak and steady state shear stress, respectively, t_h is the duration of the hold period and t_c is the characteristic time delay beyond which the strength evolves at a rate of β. In this equation β_1 and t_{c1} relate to the initial time-dependent increase in strength while β_2 and t_{c2} relate to the subsequent weakening behavior.

3.1.5 Calculating crack transmissivity

The change in fluid volume in the pore pressure pump was recorded continuously and used to determine the average flow rate over 15-minute intervals. This flow rate was based on the volume of water at room temperature and was adjusted for flow through the heated sample by

$$Q_T = Q_{22\,^\circ C}\left({}^{V_T}/_{V_{22\,^\circ C}}\right) \quad [2]$$

where Q is the volumetric flow rate and V is the specific volume of water with the subscript denoting the temperature in degrees Celsius.

We quantify the fluid transport properties of the fracture in terms of the crack transmissivity (κ_C), which is equivalent to the product of the permeability of material within a fracture and the effective thickness of the fracture (Ji et al., 2022). In our geometry, the fracture surface is approximately elliptical so the fracture width is not constant. Additionally, flow is between boreholes with centers separated by a distance, l, so flow is not parallel. We therefore use the approximation proposed by Ye & Ghassemi (2018), in which the elliptical flow region is approximated as a rectangle with area equal to that of the ellipse and a length equal to the distance between the boreholes. For a fault inclined 30° to the sample axis, this approximation yields:

$$\kappa_C \cong \frac{2l^2}{\pi D^2}\frac{\nu_f Q_T}{\Delta P_p} \quad [3]$$

where D is the minor axis of the ellipse (i.e., sample diameter), ν_f is the dynamic viscosity of water at the experiment temperature (0.135 cP at 200 ℃), and ΔP_p is the pore pressure differential across the boreholes. Analysis by Ji et al. (2022) indicates that for a 30° fault this approximation yields a crack transmissivity that is 13% below the transmissivity calculated from numerical models of elliptical flow. As we are primarily interested in relative changes in $\varkappa_C$ due to shearing or healing, absolute values of transmissivity are of less importance and the simple approximation is adequate.

3.2 Single Fracture Convergence tests

Simulated single fracture convergence tests were conducted to measure closure and actual aperture as a function of time, effective stress, temperature and initial aperture (as controlled by the surface roughness) under saturated conditions. These experiments are intended to address the fate of hydraulically generated, opening-mode fractures following the fracturing process, once the fracture-normal effective stress reverts to the ambient level at depth.

Two types of experiments were conducted: long duration blind tests where the primary data are from 3D surface profiles made before and after the experiment, and shorter duration experiments where fracture aperture and closure are monitored directly using electrical resistance.

3.2.1 Blind experiments

The two-month duration blind tests were conducted using an artificial discontinuity between two synthetic, 0.5" diameter, 0.25" thick quartz crystals. The upper sample has optically smooth, chemically polished surfaces normal to the axis (Fig. 1a). The lower sample is nearly identical with one axis-normal optical surface and another that was manufactured with an optical surface that has subsequently been roughened with grinding compound (400 or 240 grit; Fig. 1b). The lower sample has a 1/16" hole drilled along the cylinder axis to allow fluid access to the discontinuity (Fig. B3). Experiments are conducted jacketed in a hydrothermal vessel with confining fluid and pore pressure. These are plausibility tests to determine whether measurable closure occurs at conditions that approximate those at the FORGE site. Experiments were conducted at 200 °C at effective stresses between 50 and 100 MPa. An exploratory test was conducted at 300 °C and 75 MPa for comparison with deformation at lower temperature. Additionally, two control experiments, one at 200 °C dry and the other at room temperature saturated, established the necessity of elevated temperature and the presence of fluid for stress-driven permanent closure.

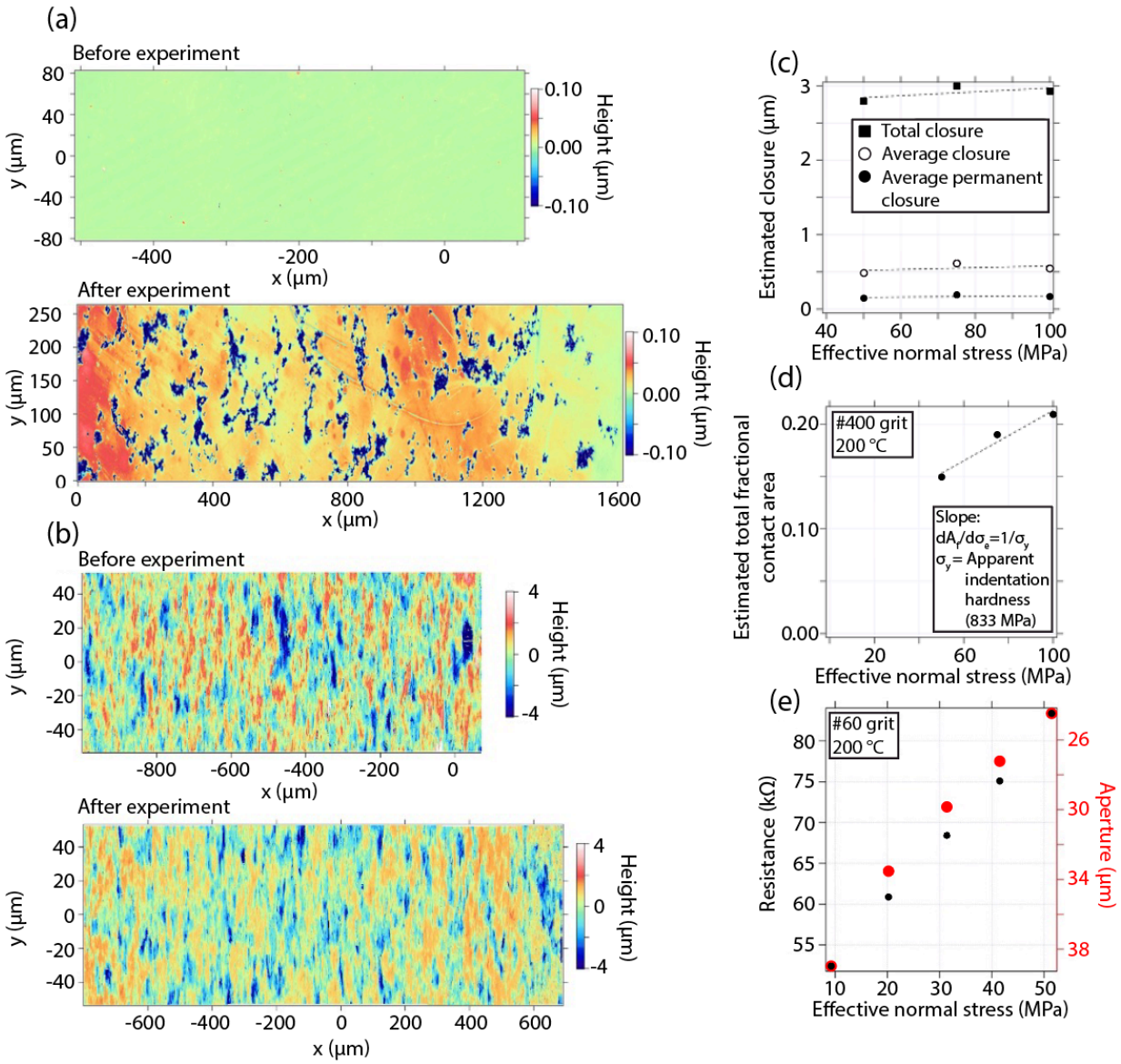

*Figure 1. Single fracture convergence tests. Topography of top **(a)** and bottom **(b)** surfaces used in the convergence tests is characterized before and after each experiment using a Zygo model 7200 white light interferometer at the University of Oregon CAMCOR facility. The upper surface **(a)** shows deformation of a #240 grit roughed by asperity indentation and the bottom surface **(b)** shows flattening of a #400 grit roughened surface. Surfaces come from two different experiments both conducted at 200 °C and 75 MPa effective normal stress. Significant closure, estimated from topography in the blind tests **(c & d)** or based on electrical resistivity measurements **(e)**, is observed in the experiments.*

This configuration of single-crystal rough and flat surfaces was selected so that closure could be measured and relatively easily interpreted from the blind tests. Simplifications associated with this geometry include: 1) that all the contacts between the surfaces are in the same known orientation in the plane of the interface, and 2) asperity contacts on the interface have uniform orientation and material properties. The crystals are transparent so that contacts on recovered

surfaces can be easily viewed with long-distance objectives being ideally oriented for transmitted and reflected light microscopy. Single crystal surfaces also lack grain boundaries that allow fluid transport out of the interface or promote preferential etching of the surfaces at elevated temperature and pressure. Moreover, a great deal of early theoretical work on contact mechanics and macroscopic mechanical properties of interfaces was developed using this rough surface on a flat geometry, e.g., elastic contact Greenwood and Williamson (1966); plastic contact Pullen & Williamson (1972), Nayak (1973).

An additional advantage to the asperities on a flat geometry is the asymmetry of the stress state across the interface that may allow access to both brittle and ductile deformation processes in the absence of shear. Immediately beneath an asperity in the flat surface, the stress state is highly confined such as beneath an indenter in a micro- or nano-indentation test (Johnson, 1985). Beneath an indenter the confinement and differential stresses are limited by the material hardness, for quartz ~ 10 GPa. In contrast, immediately above the contact the asperity is entirely unconfined and more likely to undergo brittle fracture if the contact normal stress reaches the brittle failure stress. Such unconfined asperity failure is evident as pervasive fracture wear product (fault gouge) in active natural faults (e.g., Chester et al., 2004) and in large displacement rock friction experiments.

The greatest advantage of the rough on flat surface geometry in blind experiments is the flat surface itself. This provides a pre-experiment reference with known and extremely small amplitude variation. Changes to the surface height over the experiment duration record possible dissolution, precipitation, indentation and adherence.

3.2.2 In-plane resistance

The blind experiments at elevated temperature and pressure produced deformation of the rough surface asperities and indentation of the flats, providing clear evidence of permanent interface closure and an increase in the fracture stiffness at FORGE temperatures. That milestone led to the second and third year in-plane resistance experiments. The premise of these tests is to use the saturated interface as a thin, high-resistance conductor between two electrodes, and whose thickness (aperture) is inversely proportional to measured resistance.

The technique was developed and tested initially using a series of jacketed but unconfined uniaxial plausibility tests: 1) multi-contact indentation tests using small diameter tungsten carbide spheres between saturated flat surfaces of PMMA or silica glass such that the initial thickness and resistance of the interface is known exactly and 2) uniaxial tests with the rough surface on a flat geometry used in the blind experiments (Fig. B3). Following these initial tests, experiments at room temperature and elevated confining and pore pressures were run at effective stresses up to 50 MPa. Finally, we conducted tests at 200 °C using the same configuration and sample dimensions as the blind tests: an optically smooth upper sample against a roughened surface. In these runs, the surface roughness is larger (60 or 240 grit grinding compound) than in the blind tests.

3.2.3 Experimental details

Two different vessels were used in the blind experiments, a LECO/Tempres hydrothermal vessel consisting of a passivated Rene 41 body and an Inconel 625 end plug; and a High Pressure Equipment 200 MPa vessel. The vessel is heated to run conditions using a three-zone external furnace. The experiments are raised to run conditions from an initial effective stress between 20 to 50 MPa. Effective stress is held approximately constant as the temperature is raised incrementally over a few hours. Once the temperature has equilibrated, the effective stress is raised over a few 10s of minutes to its run value. Then the temperature and effective pressure are held approximately constant for the duration of the experiment, typically two months.

For the in-plane multi-contact and other uniaxial resistance experiments the sample column is loaded using a commercial non-rotating pneumatic actuator driven by standard laboratory compressed air, pressure < 150 psi. A proportional-integral-derivative pressure controller (PID) determines the supply pressure to the actuator. The PID controls on a force feedback signal from a 5000 lb load cell in line with the actuator. The loading frame is repurposed from a 12-ton laboratory hydraulic press. To minimize misalignment the sample column is completed by a platen with a spherical seat. The load cell is mounted in the center of the frame head with a hollow nylon threaded rod through a hole in the head. Fluid, tubing and electrode access the interface through the hollow threaded rod.

The uniaxial resistance experiments are jacketed with heat shrink tubing; the jacket is bound against the lower sample half with wire below the outer electrode to block any conductance along the jacket-sample interface. The jacket seals against O-rings above and below the sample halves and the jacket is clamped against the O-rings with hose clamps. The upper cap and the upper sample have through-holes for fluid access to the interface. The fluid is held at static pressure slightly above atmospheric in an approximately 7" long sealed tube, providing a small hydraulic head. A solid 300 series stainless steel wire is inserted to the interface through the tube; the outer electrode is a sheet of 0.001" thick 300 series stainless steel shim stock.

For the confined rough surface experiments the samples are placed between the end plug and top cap. For these experiments the outer electrode consists of a 1/4” band of stainless steel shim stock that is wrapped around the bottom of the top cap, the upper sample and a portion of the lower sample. This is the outer electrode. The sample assembly is placed within heat shrink tubing (PFA in the high temperature experiments) and the tubing is shrunk to produce a snug assembly. The jacket is then clamped against the upper and lower seals with hose clamps. A stainless wire is inserted into the lower fluid port to the sample interface; this is the center electrode. A custom manifold in the pore pressure system seals a single conductor feedthrough that is connected to the wire. A similar wire inserted through the top vessel port is attached to the top cap providing electrical continuity with the outer electrode. The other end of the wire connects to an identical upper manifold and feedthrough on the confining pressure system. The sample assembly is placed and sealed in the vessel.

In all experiments to date, de-aired tap water is the pore pressure medium. The sample is evacuated with a vacuum pump for 4 hours and then saturated. The resistivity of the pore fluid is measured prior to saturation with a standard laboratory conductivity meter. Pore pressure is elevated as needed using a manual High Pressure Equipment pressure generator. Hydraulic oil or silicone oil is the confining pressure medium; confining pressure is supplied by an air-driven pump and controlled with an electronic air pressure controller mounted on an air-controlled pressure reducing regulator or with a manual regulator. Resistivity is measured using a GWINSTEK model-6300 LCR meter. These are AC resistivity measurements using a single voltage and frequency, 1 volt amplitude and 1 kHz. The resistivity reported is the equivalent circuit series resistivity, R_s.

3.2.4 Inferring closure from topography

The topography of the blind experiment quartz surface is characterized before and after the experiments using a Zygo model 7200 white light interferometer at the University of Oregon CAMCOR facility and using conventional transmitted and reflected light microscopy. Interface properties such as contact area, elastic and inelastic closure, and elastic stiffness can be estimated from topography (e.g., Abbott and Firestone, 1933; Greenwood and Williamson, 1966; Brown and Scholz, 1985). Our analyses use the difference between the initial and recovered topography to infer the permanent and recoverable deformation. Particular metrics used to determine changes in the topography are: differences in the average height of topography above the mean plane, R_a^+, differences in the Abbott-Firestone bearing ratio, and differences in a modified constant solid volume bearing ratio. Elastic interface stiffness is estimated using an approach that descends from Greenwood and Williamson (1966) and implements the actual 3D topography, tracking the compressive deformation, *L* - *d*, at each asperity. Asperities are identified from the 3D topography at each possible surface separation by a standard particle association analysis. *L* is undeformed height, and d is the surface separation. The force *F* exerted by each asperity is a function of its average deformation, $F(L-d)$. The interface normal stress at each separation is the sum of the forces exerted by all the asperties, divided by the total surface area, A,

$$\sigma_e = \frac{1}{A}\sum_{i=1}^{N} F_i(L_i - d) \qquad [4]$$

where $F_i(L-d)$ is the force exerted by asperity *i* and *N* is the total number of asperities, determined based on surface topography data exceeding the surface separation threshold. For $F_i(L-d)$ we use an elastic-kinematic method that allows elastic deformation throughout all contacting asperities. The elastic component of $F_i(L-d)$ depends on the assumed asperity shape and its height.

3.2.5 Measuring dilatant volume reduction with in-plane resistance

Measured electrical resistance, *R* (ohms), relates to material resistivity *r* (ohm m) as $R = \rho l / A_c$, where *l* is the distance between the positive and negative terminals of a resistance measuring

instrument, and A_c is the cross-sectional area of the conductor (Heaney, 2003). Our experimental geometry is a dilatant interface saturated with a conductive fluid, between highly electrically resistive and hydraulically impermeable cylindrical samples. The in-plane resistance of the interface is measured between an inner electrode inserted through the fluid port into the center of the interface, and a cylindrical metal jacket electrode on the circumference of the interface. For the circular in-plane geometry where resistance is measured from the circumference to the center hole in a disk-shaped sheet of varying in-plane thickness, resistance is

$$R = \frac{\rho}{2\pi h_*} \ln \frac{r_1}{r_0} \quad , \qquad [5]$$

where r_1 and r_0 are the outer sample radius and the radius of the sample center hole, respectively, and h_* is the harmonic average thickness of the interface. The interface normal stiffness, k, relates to measured resistance as

$$k = -\frac{R_0}{h_0} \frac{d\sigma}{dR}, \qquad [6]$$

where R_0 and h_0 are the values of resistance and harmonic aperture prior to a small step change in effective normal stress, $d\sigma$, and dR is the measured change in resistance. The great advantage of using in-plane resistance to determine interface aperture, closure and elastic stiffness is that, unlike displacement devices that are typically used to measure closure (e.g. Scholz and Hickman, 1983), in-plane resistance measures aperture directly. An additional advantage is the lack of electronic components, in principle allowing passive, accurate measurements at elevated temperature and pressure.

3.3 Forward and empirical models

Surface scans of the rough fracture samples used in the triaxial deformation tests were acquired and the scans were visually aligned. A python package was written to analyze the scanned surfaces for reproducible trends in geometry during the process of aperture closure and across stages of slip. Of particular importance is the relationship between current mean aperture and contact ratio (R = fraction of upper/lower surfaces that are in contact). If such a (shear dependent) relationship can be established, then measured permeability or a numerically evolving mean aperture is sufficient information to compute apparent stress, a primary unknown parameter in any model for asperity creep or general mechanical deformation. Classic rock mechanics literature treats aperture closure in an exponential or logarithmic fashion, along the lines of,

$$b_m = a + b \cdot e^{(-c \cdot \sigma)}, \qquad [7]$$

where b_m is mean aperture and σ is applied normal effective stress. Here we suggest this empirical form can be recast as a wrapper on a more fundamental relationship, where it is the contact area ratio that follows an exponential form and then elastic/inelastic closure depends

on this ratio via the apparent stress ($\sigma_a = \sigma/R$). In other words, mechanical aperture closure is roughly exponential because the apparent stress is roughly exponential. It has been suggested that Eq. 7 can be applied at any stage of slip with a linear (dilation-like) offset to the initial coefficients. We show this to be true, but the offset is non-linear.

To begin, we define the relationship,

$$b_m = a(x) + b(x)e^{(-R/c(x))}, \quad [8]$$

where the coefficients are now a function of current slip (x) and the dependent variable becomes contact area ratio (*R*). In our statistical analysis, aperture is computed from an adaptive three-dimensional mesh of the void space at a given state of slip and closure, as the relationship between piecewise element volume and center plane of flow. This does lead to some deviation from previous methods of point-by-point vertical offset subjected to some standard or geometric mean. We use this meshed volume definition to generate realizations of Eq. 8 as correlated surfaces are subjected to slip and closure (Fig. 2a). Other statistics are also generated, such as mean radius of the contacts, which is roughly a linear function of aperture and consistent across shear. From these realizations we then define the coefficients as functions of slip (Fig. 2b). There is some linearity to the relationships, as mentioned above. The result is an intrinsically slip-dependent relationship for contact ratio (or apparent stress once the applied stress is known) which can then feed elastic/inelastic models for asperity deformation. There are several benefits to the area-based form. First, it depends only on (initial) geometry or is well suited to be defined on statistical distributions. Second, it can track the volume of asperities that have been active in the aperture change. And lastly it can be applied to any stress-dependent mechanism, or several operating in unison.

The forward model, another python package, uses the implicit state variables (*T*, *P*, σ, *slip*) supplemented by exponential curves of contact area within the (pre-experiment) fracture profile offset non-linearly by slip on the surface (Eq. 8). This curve is then inverted to provide a value of *R* for any current value of b_m, which evolves in time via some mechanism, and thus the current apparent stress on fracture asperities is known. In the current model, b_m evolves through 1) elastic deformation using Hertzian contacts in a Newton iteration between b_m and *R*, 2) shear dilation, which is implicit to the solution of Eq. 8, and stress activated creep. In rare cases temperature and chemical potential have been added to Eq. 7 as additional exponential multipliers. Here, creep follows an Arrhenius (*T*) dependent general reaction rate and an exponential dependence on apparent stress. The result is a mechanism that adapts implicitly to any current state of temperature and bulk stress. We have also run this model using a Finite Element Model solution for diffusion- dissolution creep (Taron and Elsworth 2010), although diffusion was not shown to be a significant rate-limiter in our experiments.

In an alternative complementary approach, we applied permeability models that empirically follow two-stage reaction rates observed in the experiments; a long-term (power-law) rate of degradation and a short-term (exponential) rate that is a function of *time-since-slip*. For reservoir scale implementation, application of the two-stage model is automatic within the

OGSn (Taron et al. 2016) simulator, which detects a new slip regime based on the rate of slip (*dslip/dt*) and resets the secondary healing rate. These results do not rely upon a fracture profile but are instead tuned to observed (short- and long-term) rates of healing.

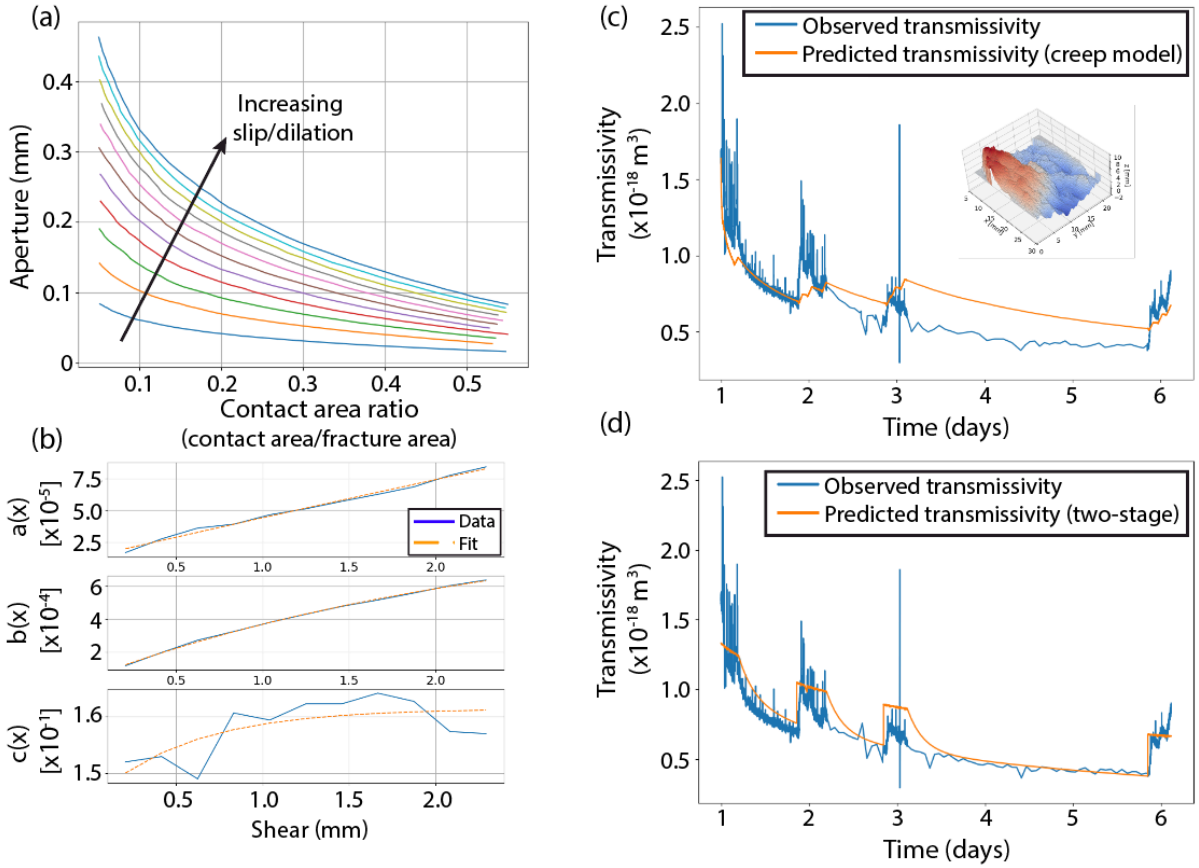

Figure 2. (a) Example of fits of fractional contact area relative to current mean aperture based on surface scans of samples used in rough fracture experiments. (b) By compiling exponential fits, shown in Fig. 2a, for all values of slip to generate a single exponential model (eq. 7) with coefficients that are a function of slip. (c) Forward prediction from creep model and (d) application of two-stage rate model are shown in comparison to data from an experiment at 200 °C. An image of this fracture surface is shown in the inset on fig. 2c and provided in Fig. B2.

4 Results and Discussion

4.1 Key Results

4.1.1 Evolution of Fracture strength

In our triaxial shear experiments we examined both the evolution of frictional strength and crack transmissivity in smooth fractures. In the rough fracture experiments only the evolution of fluid transmissivity was examined as the strength evolution is highly dependent on characteristics of the surface contacts (e.g., interlocked asperities). Clear evidence of time-dependent strengthening or weakening is not observed in the rough fracture experiments (Fig. B4).

Experiments on smooth fractures confirmed the overall dependence of fault strength on the logarithm of hold time. However, the details of temperature dependence are complex. At room temperature the peak strength observed upon resumption of sliding on the fault surface is followed by a rapid return to steady-state sliding friction (Fig. 3a). The change in strength increases with the logarithm of hold time has been previously observed. However, when temperature was increased, the peak strength measured when shearing resumed after a long hold (≥ 1000 s) was less than the steady-state strength measured at the end of the previous slide period and, for Westerly granite and UF10, significant shear displacement was required for the steady-state strength to approach the pre-hold value (Fig. 3b).

The change in frictional strength ($\Delta\mu$) was determined from these data shows a transition from time-dependent strengthening to time-dependent weakening (Fig. 3c). The timing of this transition varies with temperature, occurring earlier at higher temperatures. Additionally, comparison of the no flow and flow-through experiments reveals a difference in the onset time of weakening. The transition tends to occur significantly earlier in the flow-through experiments than in the no flow experiments, except at 250 °C where both flow conditions have similar transition times.

The rates of strength evolution were quantified using Eq. 1 as described in Jeppson et al. (2023). In the no flow tests, initial time-dependent strengthening is clearly observed at temperatures ≤ 200 °C with initial healing rates of 0.005, 0.006, and 0.008 per e-fold at 22, 100, and 200 °C, respectively, with cutoff times on the order 1–10 s. Experiments at 250 °C lacked sufficient data to constrain the initial strengthening rate. As the rates at lower temperatures are consistent with sub-critical crack growth (e.g., Mitchell et al., 2013), which is an Arrhenius process, we extrapolate that β_1 and t_{c1} at 250 °C are 0.008 and 9 s, respectively. The process controlling time-dependent weakening under the no flow condition appears to be too sluggish to be constrained at temperatures ≤ 200 °C. Fitting the data at the higher temperatures yields β_2 of -0.051 and -0.020 and t_{c2} of $2\text{x}10^5$ s and 346 s at 200 and 250 °C, respectively.

In the flow-through tests the weakening process dominates at temperatures < 100 °C, likely masking strengthening that occurs at short timescales. At 22 °C, the flow-through tests yield β_1 and t_{c1} of 0.004 and 21s, respectively, similar to that measured under the no flow condition. We assume that the initial strengthening process during the flow-through tests is the same as that operating during the no flow tests. With β_1 and t_{c1} constrained, fitting the data yields β_2 of -0.049, -0.014, and -0.015 at 100, 200, and 250 °C, respectively. The associated characteristic delay time (t_{c2}) decreases with temperature from $4\text{x}10^4$ s at 100 °C to 117 s at 250 °C.

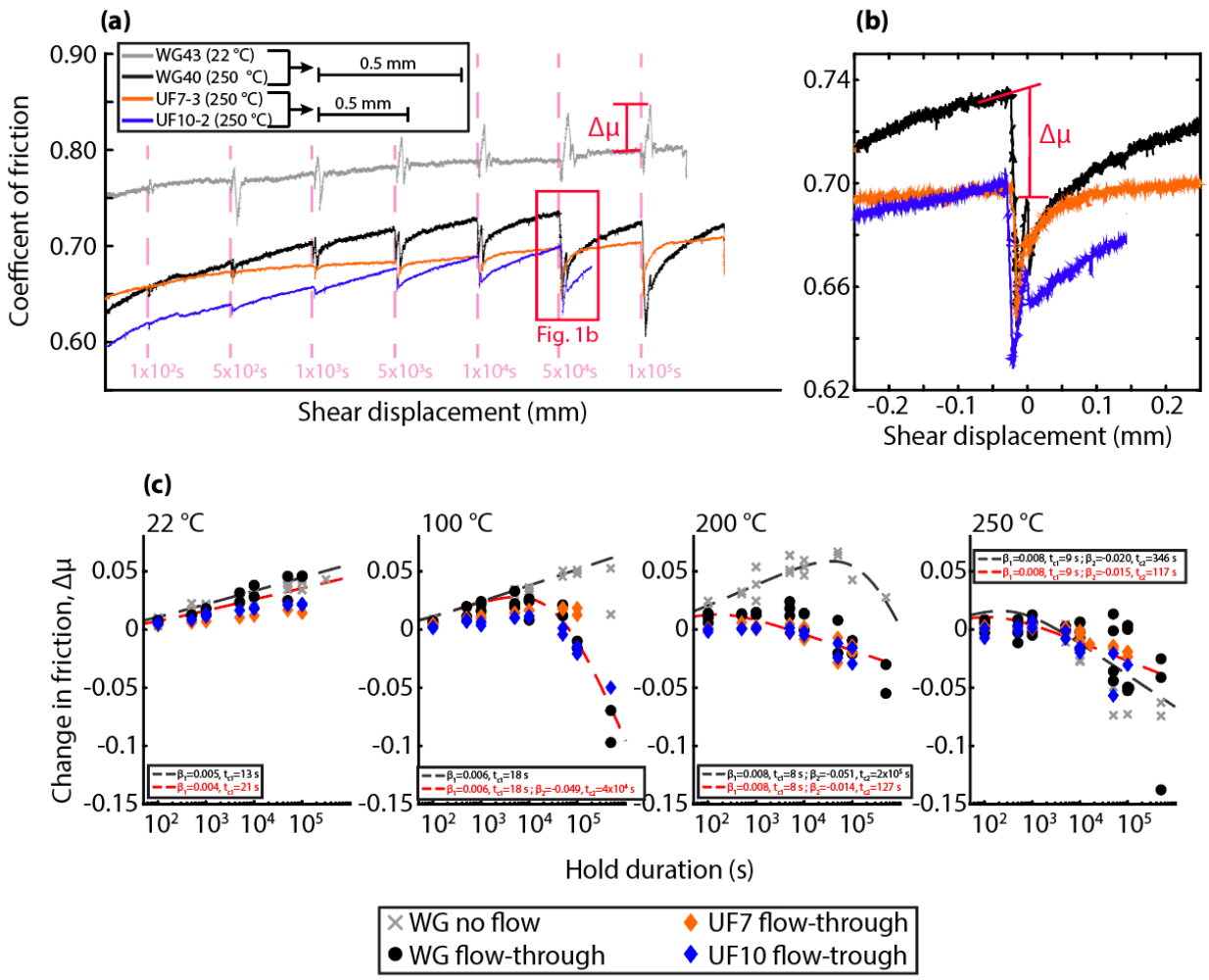

Figure 3. Triaxial shear experiments. ***(a)*** *Evolution of the coefficient of friction with shear displacement during representative tests on smooth fractures in Westerly granite and Utah Frontier Observatory for Research in Geothermal Energy (FORGE) core samples. Locations of hold periods are indicated by the pink dashed lines with durations shown.* ***(b)*** *Comparison of changes in friction associated with at 500,000s hold at 250 °C measured for samples of Westerly granite (black) and Utah FORGE samples UF7 (orange) and UF10 (blue). Experiments showed significant weakening during the hold.* ***(c)*** *Change in friction with hold duration measured at temperatures from 22 to 250 °C for both no flow (x's) and flow-through (solid symbols) conditions.*

While the initial strengthening behavior is consistent with a process such as subcritical crack growth, the mechanism responsible for the weakening is still under investigation. We find clear evidence of secondary mineral phases developing at elevated temperatures (Fig. B5). If these phases are weak, they could result in reduced friction (even at low concentrations) if formed preferentially at load-bearing contacts. This would also encourage localized flow occlusion and is a subject for future investigation.

4.1.2 Evolution of crack transmissivity

The initial crack transmissivity measured at room temperature (22 °C) on undeformed smooth fractures ranges from 1.5×10^{-18} to 2.3×10^{-16} m^2 for Westerly granite samples and from 4.8×10^{-19} to 6.3×10^{-17} m^2 in the samples taken from the Utah FORGE core. Initial crack transmissivity in the rough fractures in Westerly granite tends to be higher, only ranging from 3.0×10^{-17} to 5.4×10^{-16} m^2. Raising the temperature tends to have a limited effect on the initial (unsheared) transmissivity, generally resulting in reductions less than an order of magnitude.

Shear displacement has a greater impact on the transmissivity. After ~ 1 mm of shear displacement the crack transmissivity had been reduced by an order of magnitude or more and ranged between 2.8×10^{-20} and 3.0×10^{-17} m^2. The sheared crack transmissivity was highest in the rough fracture samples falling between 5.4×10^{-18} and 3.0×10^{-17} m^2. Initially the transmissivity follows an approximately linear trend in a log-log plot but after ~2 - 3 hours (~ 1.8 mm slip) the curves transition towards slower decay. The initial rapid reduction in crack transmissivity due to shear is consistent with previous work on Coulomb materials (Im et al., 2019) and reflects the effects of mechanical processes such as shearing of surface asperities and development and comminution of wear products. Following the initial rapid decrease due to shearing, the transmissivity generally exhibits continuous decay over the progression of the experiments but superimposed on this decay are transient increases in transmissivity during periods of shear slip (Fig. B6). This long-term rate of decay can be described by a power-law relation:

$$Q_r = Ct^{R_p} \quad [9]$$

where C is a fitting constant, t is the time since the start of the experiment, and R_p is the power exponent, which describes the time-dependent evolution of transmissivity.

Comparing the power exponents determined for both smooth (Westerly granite & Utah Forge samples) and rough fractures the rate of decay generally increases as temperature increases up to 200 °C (Fig. B7). However, at 250 °C the rate of reduction decreases and sometimes indicates enhancement of transmissivity instead of reduction. This potential enhancement is also observed with sample UF10 at 200 °C. Additionally, the smooth fracture surface in Westerly granite at 250 °C exhibits a nearly constant to slightly increasing transmissivity with time for the first ~57 hours, at which point there is a rapid reduction followed by a more gradual decay in transmissivity. Further experiments on other Westerly granite samples showed that this rapid reduction was repeatable but also recoverable if flow direction or pore pressure was changed. Both the enhancement of transmissivity and rapid reduction at 250 °C may be related to the flow condition used in these experiments. In the flow-through tests fresh pore fluid, that is undersaturated with respect to the minerals present in the rock sample, is constantly being introduced into the fracture. This chemical disequilibrium can lead to enhanced crack transmissivity due to surface dissolution (Detwiler, 2008). Such dissolution can lead to increased stress at contacting asperities which eventually fail, resulting in a nearly instantaneous reduction in transmissivity (Detwiler, 2008).

Transient increases in transmissivity that occur during sliding periods are due to shear dilation (Im et al., 2019). When shear displacement is halted transmissivity decay occurs rapidly, quickly transitioning back to the background decay rate. The difference in decay rates suggests that when the gouge is driven far from equilibrium by active shearing, its densification may be dominated by a different mechanism from long-term compaction. When the background, long-term decay trend is removed the residual, short-term transient decay signal exhibits an exponential decay rate that slows as temperature increases Fig. B7. This temperature dependance suggests dissolution of fine gouge particles may counteract the reduction of transmissivity due to compaction.

Pore fluid samples, taken periodically throughout the experiments, provide data on changes in pore fluid composition (Fig. B8). Concentrations of most cations show an initial increase relative to original concentrations in the deionized water added to the system. Some cation concentrations remain relatively constant after this initial increase (SiO_2, K, Al) while others tend to decrease with time (Fe, Mg, Na). For some cations this decrease indicates that ions adhered to grain boundaries have been flushed from the system (e.g. Na) but for other cations (e.g. Fe) this suggests that fluid-rock interactions are occurring during these experiments with initial dissolution turning to precipitation as the flow rate decreases.

4.1.3 Fracture convergence

The blind tests show significant closure at the heat reservoir temperature at FORGE (200 °C) over a relatively short time of two months; the average permanent closure is 10's of percent of the average initial aperture (Fig. 1c, d). However, the effective stress in these experiments is higher (50 to 100 MPa) than in the reservoir, and these are initially very narrow fractures relative to industrial hydro-fractures.

Solute mobility is apparent on the recovered flat surfaces and there is evidence of cementation around asperities on the interface; we didn't anticipate this. The deformation is partitioned predominantly into the unconfined asperities, suggesting the closure is related to brittle failure rather than ductile or pressure solution yielding of the flat surface - this is somewhat speculative, however. Asperity deformation, closure, contacting area and cementation all increase markedly between 200 and 300 °C.

Using in-plane electrical resistance to measure fracture aperture and monitor closure worked much better than expected (Fig. 1e). The technique appears reproducible and stable, and it is simple to implement. The resolution is at a sub-micron scale at worst and may routinely approach 10's of nm.

4.1.4 Micromechanical models

4.1.4.1 Creep model

Observed (pre-slip) flow rates are in reasonable agreement but slightly lower than those predicted from mean aperture, as determined from surface profiles. This may indicate additional deformation beyond a Hertzian/Boussinesq model or most likely unaccounted thermal expansion. Forward prediction of aperture evolution from the creep model shows reasonable agreement with the observed rates of healing and magnitudes of dilation across periods of slide and hold (Fig. 2c). For long hold periods, there is disagreement between the simulated and observed transmissivity indicating that there is a secondary, long-term rate of healing that is unaccounted for in the creep model. The unaccounted secondary healing rate exhibits a progressive reduction in dilation angle beyond what the geometry predicts. We hypothesize that this is due to generation of wear products in the experiments which is not accounted for in the models although it may have other origins.

4.1.4.2 Empirical model

The two-stage empirical model reliably captures the observed experimental behavior (Fig. 2d). The strong adherence of healing rate to the two-stage degradation across all stages of slip (the full experiment) is an interesting result. This suggests that, at a single state of stress, the healing rate does not depend on the overall magnitude of slip or the amount of time that the system has been at temperature. In EGS this suggests that the age of the reservoir and/or number of stimulation events will potentially not occlude the rate of healing. However, this is based on experiments with durations of a month or less that have undergone less than 1 cm of shear displacement. If, over time, significant deformation or alteration (e.g. development of thick gouge zones or changes in mineral composition) occurs in an EGS reservoir, altering its properties, a change in the healing rate would likely be observed.

4.1.5 Simulator application

In addition to stress and slip driven evolution, bulk chemical behaviors are of interest particularly at reservoir scale. We have incorporated the reaction simulator phreeqc, via the phreeqcRM module, into OGSn. It operates in a Picard iteration with the matrix or matrices solving the balance of energy, mass and momentum. Exchange between reaction and transport occurs via source terms discretized into the governing equations with source terms that incorporate mass loss from an asperity degradation model and accommodating transport of secondary aqueous species computed from the mineral assemblage. In an environment of net dissolution, at experimental scale on the order of days, the bulk behaviors are not particularly important. If, however, significant mass loss occurs at contacting asperities, it could lead to interesting bulk observations and this is an interesting topic for future investigation. In bringing our observations and modeling to reservoir scale, it is not reasonable to operate directly on fracture surfaces and the empirical models discussed above do not require it. The empirical models are in fact designed for reservoir simulation. For this report, however, it makes sense to conduct simulations that operate directly on fracture surfaces.

Using pointwise interpolation of aperture from the surface analyzer package, we apply the two-state empirical model discussed above to execute simulations on the same fracture profile that was used to generate Fig. 2 and slip is imposed to follow precisely the experimental conditions.

Slip events trigger re-interpolation of fracture data to the mesh and a new (second-stage) healing regime. In Fig. 4 we show the (nodal-solution) velocity profile within the fracture at three slip regimes (just prior to the first three slip events in Fig. 2d). Each part of Fig. 4 is a snapshot at a different time and slip offset. In each image the fracture has also healed; the results are continuous in the healing process. While each slip event has increased aperture via dilation, the total aperture change is still negative: *healing has more than reversed the dilation*. At the times and displacements shown in Fig. 4b and 4c, aperture reduction is, despite the intervening slip event, roughly the same, but the surface is quite different. The results of this analysis demonstrate the successful discretization of realistic, empirical rate models.

4.2 Implications of Findings for Utah FORGE and EGS Technologies

At Utah FORGE and in EGS generally it is important to understand how fracture systems will behave over time and in response to processes such as shear dilation and fluid-rock interactions. Of particular interest is how permeability evolves with fault displacement and the effect of chemical interactions over time. Crack transmissivity data showed that shear dilation causes transient increases in transmissivity, but the system is dominated by an overall decrease in transmissivity with time. However, in some experiments conducted at 200 & 250 °C the rate of decay was slower and occasional enhancement in transmissivity with time was observed. This result suggests that adding fluid that is undersaturated with respect to the rock minerology may help to enhance transmissivity at elevated temperatures.

The factors controlling seismic and aseismic behavior at geothermal conditions are also very relevant in EGS. Weakening observed in triaxial shear experiments at elevated temperatures may facilitate aseismic creep that, in turn, could reduce sealing, helping to keep fractures in EGS open. Additionally, if deformation is being accommodated through aseismic creep the weakening behavior would likely result in less seismicity in granitic reservoirs relative to reservoirs in rock types where weakening is not observed (e.g. quartzite).

Additional insight on sustaining permeability in geothermal reservoirs is provided by our blind convergence experiments. Significant closure in these experiments at reservoir temperatures suggests limits on small aperture fractures within the enhanced reservoir fracture network. However, such fracture closure is driven by the effective stress and therefore would be counteracted by conducting the heat mining operation at elevated pore pressure in the reservoir.

The results of the blind experiments motivated additional single contact experiments to better establish the rates of solute transport associated with fracture healing in quartz (refer to Supplementary Document C1). We failed to measure overgrowths at 200 °C in a two-month experiment, so the rates are very slow, suggesting more quantitatively that quartz mobility at reservoir conditions should not be an issue for the reservoir viability. In a successful contact overgrowth experiment at 300 °C, the rate of fracture healing is generally very slow and appears to be controlled at this and lower temperatures by the precipitation reaction kinetics, rather than the transport step (diffusion or advection). This simplifies the modeling of fracture healing.

Our results show that the predictive creep model generally reproduces observed behavior across stages of healing and slip but does not fully capture the cumulative decay observed in our experiments. It is, nonetheless, valuable in its ability to adapt within an assumption or distribution of fracture surface statistics to any condition of temperature and stress and in its intrinsic computation of mass flux from contacting asperities. The two-stage empirical model provides a realistic rate model that can be incorporated into OGSn and used in reservoir simulations to improve predictions of permeability evolution in EGS.

4.3 Limitations/Lessons Learned

The significance of the rates and cutoff times describing the evolution of shear fracture strength is limited, as the parameters are interdependent, and none are well constrained. This empirical relation could be improved with additional measurements to define the underlying mechanisms and inclusion of expected rates for those mechanisms. It is apparent that in polymineralic hydrothermal systems the evolution of frictional strength with time and temperature is complex because of the interactions among multiple mechanisms.

There are operational limitations to measuring fracture aperture with in-plane electrical resistance: 1) This technique requires the material bounding the fracture to have low resistivity. In practice even saturated undamaged crystalline rock may be too conductive to resolve the necessary interface resistance. 2) The technique relies on knowing the material resistivity (r, in ohm m) of the fluid and that it remains stable over time. This may be a problem at elevated temperature and pressure and is the primary source of uncertainty in the aperture measurements. This might be addressed by monitoring resistivity periodically using an independent method.

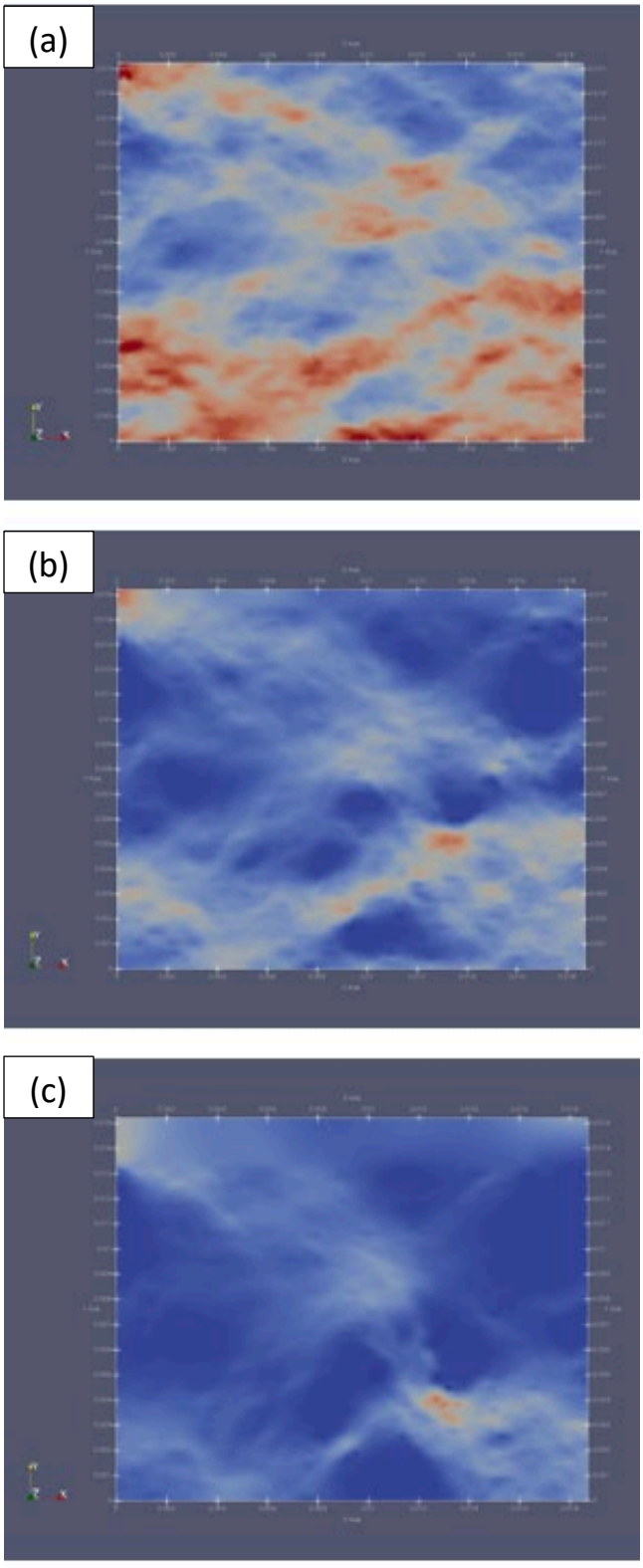

Figure 4. Velocity profile (nodal) within simulations (OGSn) using the two-stage healing model. Each snapshot is at a different time and slip offset with (a) Time = 1 day, aperture reduction = 0%, (b) Time = 1.9 days, aperture reduction = 25%, and (c) Time = 2.8 days, aperture reduction = 25% (where "aperture reduction" refers to the mean value as reduction since 1 day, or the top image).

5 Conclusions and Recommendations

5.1 Summary of Conclusions

A transition to time-dependent weakening has not previously been reported for granite at room temperature under either saturated or nominally dry conditions, or at elevated temperatures under nominally dry conditions. We

conclude that the higher-temperature weakening behavior observed in this study is caused by a mechanism that is temperature-dependent, requires the presence of liquid-phase water, and is chemically complex.

Significant closure was observed in fracture convergence tests, but this closure appears to be dominantly related to brittle failure driven by effective stress rather than ductile or pressure solution yielding of the flat surface, indicating it could be counteracted by conducting the heat mining operation at elevated pore pressure in the reservoir. Additionally, we have shown that in-plane electrical resistance can be used to measure fracture aperture and monitor closure, although this is likely of limited applicability outside of a controlled laboratory setting.

Models match general trends observed in experiments. Forward predictions are transferrable across conditions, and two-stage models are in good agreement at experimental conditions. Overall, the observed behavior does appear to depend on rates of dilation counteracted by elastic compression and creep but must be augmented by a reactive wear process.

5.2 Recommendations for Future Work

The work performed in this study has provided insight into the evolution of fractures at geothermal conditions. However, it has also highlighted areas where additional study could be beneficial. Further investigation through continued experimental and simulation efforts into the underlying mechanisms responsible for the frictional weakening observed during the triaxial experiments could clarify the implications of this result at longer time scales and reservoir scales. Additionally, these experiments were all conducted for an end-member case with deionized water as the pore fluid. As chemical processes are very important in EGS, additional experiments using brines as pore fluid could help shed light on how pore fluid chemistry affects in situ fracture evolution. Additionally, future convergence experiments incorporating flow-through could further clarify the impact of variations in pore fluid chemistry.

Tables

Table 1. Uploaded Geothermal Data Repository (GDR) Datasets and published papers. FORGE = Frontier Observatory for Research in Geothermal Energy.

GDR datasets		
Submission date	**Title**	**Link**
3 August 2022	Utah FORGE hydrothermal friction-hydraulic transmissivity laboratory experiments	https://gdr.openei.org/submissions/1406
13 April 2023	Laboratory experiments examining the effect of thermal and mechanical processes on hydraulic transmissivity evolution	https://gdr.openei.org/submissions/1493
21 December 2023	Utah FORGE: Slide-hold-slide experiments on Westerly Granite at temperatures up to 250 °C	https://gdr.openei.org/submissions/1569

Table 2. List of presentations/publications. AGU = American Geophysical Union.

Date	**Title**	**Conference/Journal**	**DOI**
February 2021	Evolution of fluid transmissivity and strength recovery of shear fractures under hydrothermal conditions	Proceedings of the 46th Stanford Geothermal Workshop	---
June 2021	Strength recovery and sealing under hydrothermal conditions	Proceedings of the 55th U.S. Rock Mechanics/Geomechanics Symposium	---
December 2021	How stress affects restrengthening in simulated fault gouge	AGU Fall meeting	---
December 2021	Variations in frictional restrengthening at hydrothermal conditions	AGU Fall meeting	---
February 2022	Impact of fluid-rock interaction on strength and hydraulic transmissivity evolution in shear fractures under hydrothermal conditions	Proceedings of the 47th Stanford Geothermal Workshop	---
March 2022	Impact of fluid-rock interaction on strength and hydraulic transmissivity evolution in shear fractures under hydrothermal conditions	GeoPRISMS, Structure and Deformation at Plate Boundaries	---

April 2022	Complexities in fault healing	University of Oklahoma, Shell Colloquium Series	---
August 2022	Impact of fluid-rock interaction on strength and hydraulic transmissivity evolution in shear fractures under hydrothermal conditions	Gordon Research Conference on Rock Deformation	---
November 2022	Impact of fluid-rock interaction on strength and hydraulic transmissivity evolution in shear fractures under hydrothermal conditions	Conference on Coupled Processes in Fractured Geological Media	---
December 2022	Impact of fluid-rock interaction on strength and hydraulic transmissivity evolution in shear fractures under hydrothermal conditions	AGU Fall meeting	---
February 2023	Effect of thermal and mechanical processes on hydraulic transmissivity evolution	Northern California Earthquake Hazards Workshop	---
February 2023	Effect of thermal and mechanical processes on hydraulic transmissivity evolution	Proceedings of the 48th Stanford Geothermal Workshop	---
December 2023	Evolution of fluid flow in rough fractures at hydrothermal conditions	AGU Fall meeting	---
December 2023	Impact of fluid-rock interactions on frictional strength in shear fractures under hydrothermal conditions	AGU Fall meeting	---
2023	Strength recovery in quartzite is controlled by changes in friction in experiments at hydrothermal conditions up to 200 °C	Journal of Geophysical Research Solid Earth	10.1029/2022JB025663
2023	Time-dependent weakening of granite at hydrothermal conditions	Geophysical Research Letters	10.1029/2023GL105517
August 2024	Interseismic evolution of fault strength	Gordon Research Conference on Rock Deformation	---

References

Abbott, E.J., & Firestone, F.A. (1933). Specifying surface quality: a method based on accurate measurement and comparison, Mechanical Engineering, 55: 569–572.

Allis, R., & Moore, J.N. (2019), "Geothermal Characteristics of the Roosevelt Hot Springs System and Adjacent FORGE EGS Site, Milford, Utah", Miscellaneous Publication 169, Utah Geological Survey, 307 pps. https://doi.org/10.34191/MP-169

Brown, S.R., & Scholz, C.H. (1985), Closure of random elastic surfaces in contact, J. Geophys. Res., 90, 5531-5545

Chester, F. M., Chester, J. S., Kirschner, D. L., Schultz, S. E., & Evans, J. P. (2004). Structure of large-displacement, strike-slip fault zones in the brittle continental crust, in Rheology and Deformation in the Lithosphere at Continental Margins, G. D. Karner, B. Taylor, N.W. Driscoll, and D. L. Kohlstedt (Editors), Columbia University Press, New York, New York.

Detwiler, R. L. (2008). Experimental observations of deformation caused by mineral dissolution in variable-aperture fractures. Journal of Geophysical Research: Solid Earth. 113(B8). https://doi.org/10.1029/2008JB005697

Greenwood, J. A., & Williamson, J. (1966), Contact of nominally flat surfaces, Proc. R. Soc. London, Ser. A, 295, 300 – 319.

Heaney, M.D., (2003), Electrical Conductivity and Resistivity, in "Electrical Measurement, Signal Processing, and Displays", Ed. John G. Webster. CRC Press, Chapter 7, 14pps.

Im, K., Elsworth, D. & Wang, C. (2019). Cyclic Permeability Evolution During Repose Then Reactivation of Fractures and Faults. J. Geophys. Res. Solid Earth 124, 4492–4506.

Jeppson, T. N., Lockner, D. A., Beeler, N. M., & Moore, D. E. (2023). Time-dependent weakening of granite at hydrothermal conditions. Geophysical Research Letters, 50(21). https://doi.org/10.1029/2023GL105517

Ji, Y., Hofmann, H., Rutter, E. H., Xiao, F., & Yang, L. (2022). Revisiting the evaluation of hydraulic transmissivity of elliptical rock fractures in triaxial shear-flow experiments. Rock Mechanics and Rock Engineering. 55, 3781-3789.

Johnson, K. L. (1985). Contact Mechanics. Cambridge University Press. 452pp.

Mitchell, E. K., Fialko, Y., & Brown, K. M. (2013). Temperature dependence of frictional healing of Westerly granite: Experimental observations and numerical simulations. Geochemistry, Geophysics, Geosystems, 14(3), 567–582. https://doi.org/10.1029/2012GC004241

Nayak, P.R., (1973), Random process model of rough surfaces in plastic contact, Wear, 26, 305–333.

Polak, A., Elsworth, D., Yasuhara, H., Grader, A. S. & Halleck, P. M. (2003). Permeability reduction of a natural fracture under net dissolution by hydrothermal fluids. Geophys. Res. Lett. 30.

Pullen, J., & Williamson, J.B.P. (1972), On the plastic contact of rough surfaces, Proc. Roy. Soc. A., 327, 159-173.

Scholz, C. H., & Hickman, S. H. (1983), Hysteresis in the closure of a nominally flat crack, J. Geophys. Res., 88(B8), 6501–6504, doi:10.1029/JB088iB08p06501.

Taron, J., Ingebritsen, S. E., Hickman, S. & Williams, C. (2016). Dynamics of permeability evolution in simulated geothermal reservoirs. in Crustal Permeability (eds. Gleeson, T. & Ingebritsen, S. E.) 363–372.

Taron, J. & Elsworth, D. (2010). Constraints on compaction rate and equilibrium in the pressure solution creep of quartz aggregates and fractures: Controls of aqueous concentration. J. Geophys. Res. Solid Earth, 115, 1–17.

Tembe, S., Lockner, D., & Wong, T.-F. (2010). Effect of clay content and mineralogy on friction sliding behavior of simulated gouges: Binary and ternary mixtures of quartz, illite, and

montmorillonite. J. Geophys. Rex. Solid Earth. 115. https://doi.org/10.1029/2009JB006383
Ye, Z., & Ghassemi, A. (2018). Injection-induced shear slip and permeability enhancement in granite fractures. Journal of Geophysical Research: Solid Earth. 123(10). https://doi.org/10.1029/2018JB016045

Appendices

A. Data Tables

Table A1. Average rate constants determined from triaxial shear experiments.

Temperature (°C)	**Flow condition**	**β_1**	**t_{c1} (s)**	**β_2**	**t_{c2} (s)**	**Power law exponent (R_p)**
22	No flow	0.005	13	---	---	
100	No flow	0.006	18	---	---	
200	No flow	0.008	8	-0.051	$2x10^5$	
250	No flow	0.008	9	-0.020	346	
22	Flow-through	0.004	21	---	---	-0.35
100	Flow-through	0.006	18	-0.049	$4x10^4$	-0.50
200	Flow-through	0.008	8	-0.014	127	-0.46
250	Flow-through	0.008	9	-0.015	117	-0.08

Table A2. Triaxial shear experiments performed on Westerly granite samples

Experiment	**Temperature (°C)**	**Fracture surface**	**Flow condition**
WG20	200	Smooth (#240 grit)	Flow-through
WG21	200	Smooth (#240 grit)	Flow-through
WG22	200	Smooth (#240 grit)	No flow
WG34	22	Smooth (#240 grit)	No flow
WG35	100	Smooth (#240 grit)	Flow-through
WG36	250	Smooth (#240 grit)	No flow
WG38	22	Smooth (#240 grit)	No flow
WG39	100	Smooth (#240 grit)	No flow
WG40	250	Smooth (#240 grit)	Flow-through
WG41	22	Smooth (#240 grit)	Flow-through
WG43	22	Smooth (#240 grit)	Flow-through
WG44	250	Smooth (#240 grit)	Flow-through
Frac8	200	Rough	Flow-through
Frac9	250	Rough	Flow-through

Frac10	100	Rough	Flow-through
Frac11	22	Rough	Flow-through
Frac13	250	Rough	Flow-through

Table A3. Triaxial shear experiments performed on samples from Utah FORGE well 16A(78)-32. All experiments were performed on smooth surfaces roughened with #240 grit under the flow-through condition. FORGE = Frontier Observatory for Research in Geothermal Energy

Experiment	**Rock type**	**Measured depth (ft)**	**Temperature (°C)**
UF7-1	Biotite-rich banded gneiss	10957.8	250
UF7-2	Biotite-rich banded gneiss	10957.8	200
UF7-3	Biotite-rich banded gneiss	10957.8	250
UF7-4	Biotite-rich banded gneiss	10957.8	100
UF7-6	Biotite-rich banded gneiss	10957.8	22
UF10-2	Quartz-rich granitoid	10975.2	250
UF10-3	Quartz-rich granitoid	10975.2	200
UF10-4	Quartz-rich granitoid	10975.2	100
UF10-6	Quartz-rich granitoid	10975.2	22

B. Additional Figures

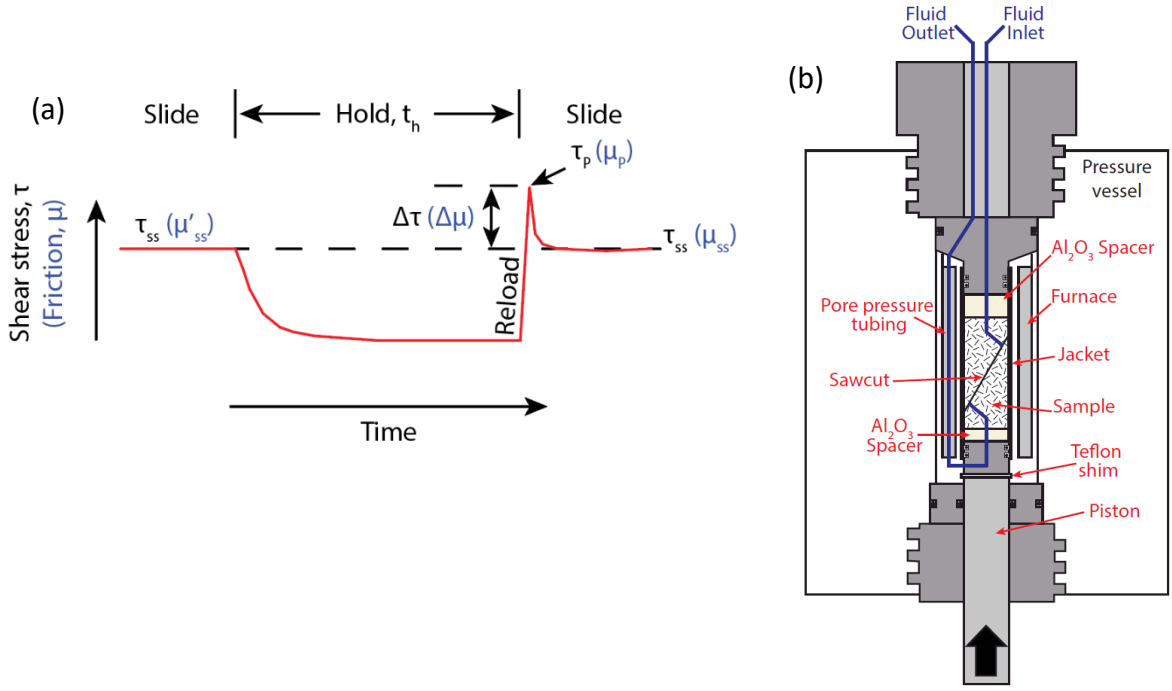

Figure B1. (a) Schematic diagram of the evolution of shear stress or friction during slide-hold-slide tests. The shear stress evolution before, during, and after a hold period (t_h) is shown. The changing in friction, $\Delta\mu$, is quantified by the difference between failure strength (μ_p) upon reloading the sample after the hold and steady-state shear strength (μ_{ss}) prior to the hold. (b) Schematic of the triaxial apparatus and sample geometry used in this study. Black arrow indicates loading direction.

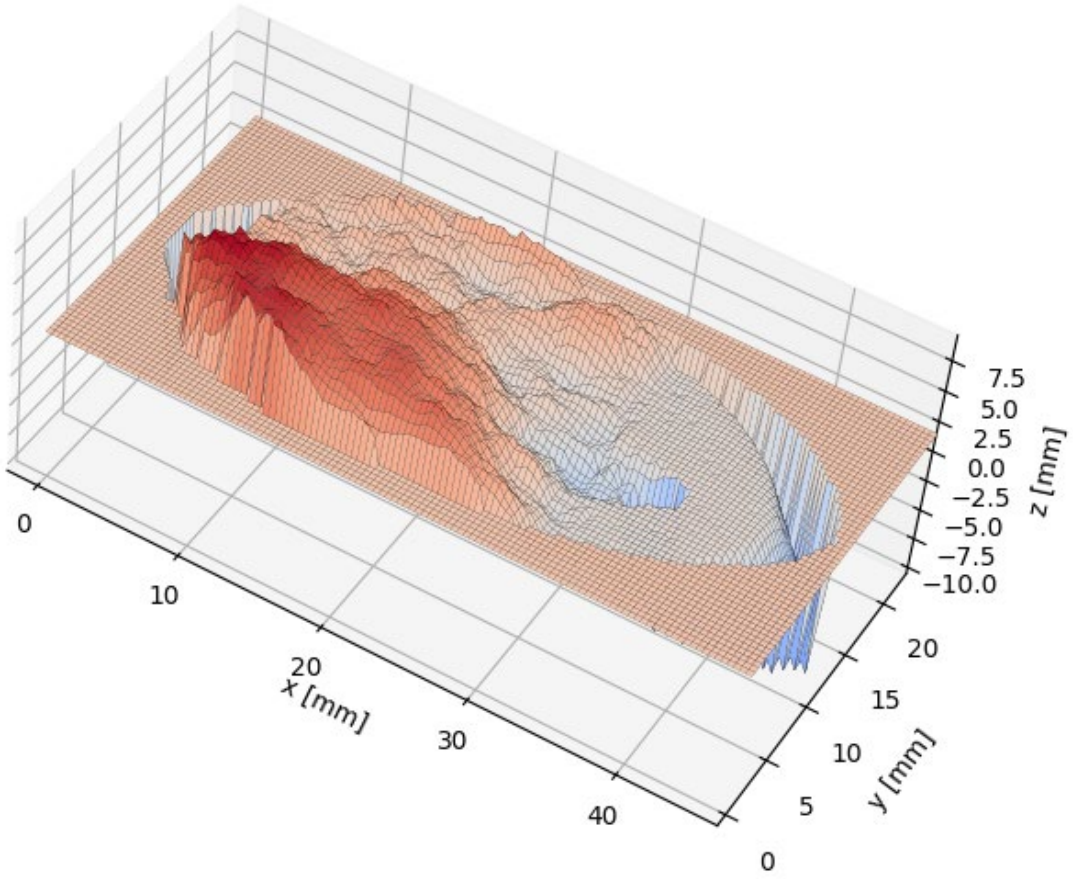

Figure B2. Example of rough fracture surface. Data shown are from a pre-shear scan of the Frac8 sample.

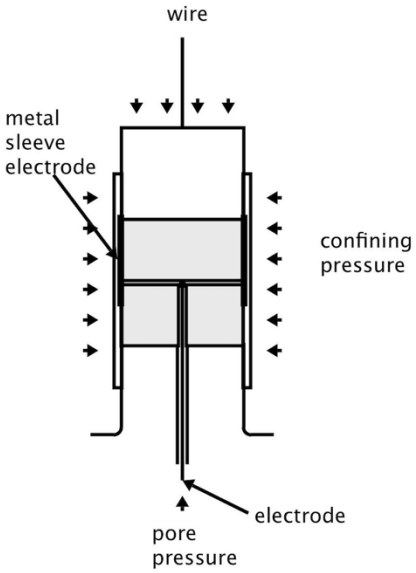

Figure B3. Schematic of the sample geometry used in the single fracture convergence tests.

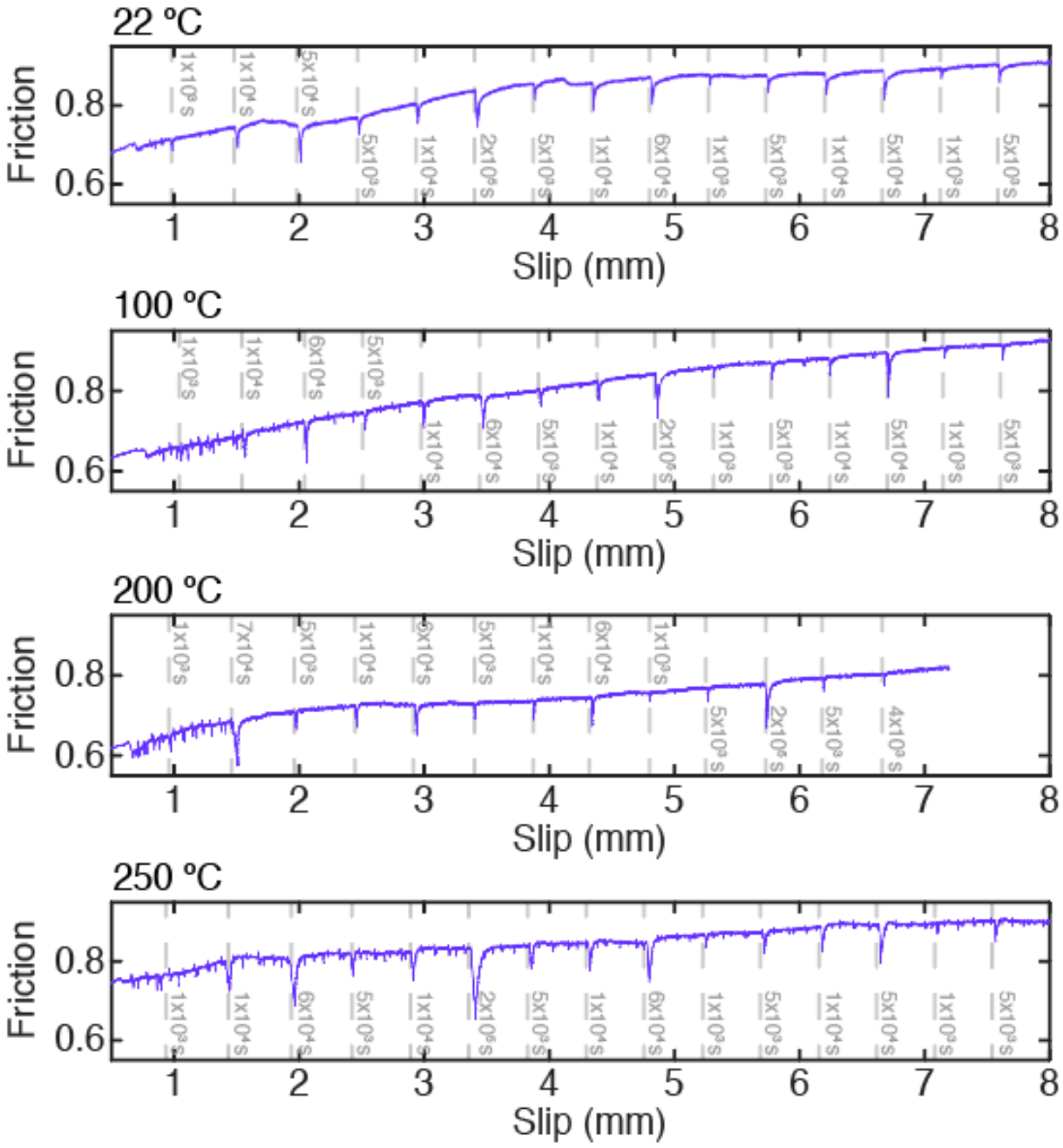

Figure B4. Evolution of friction with shear displacement during experiments performed on rough fractures.

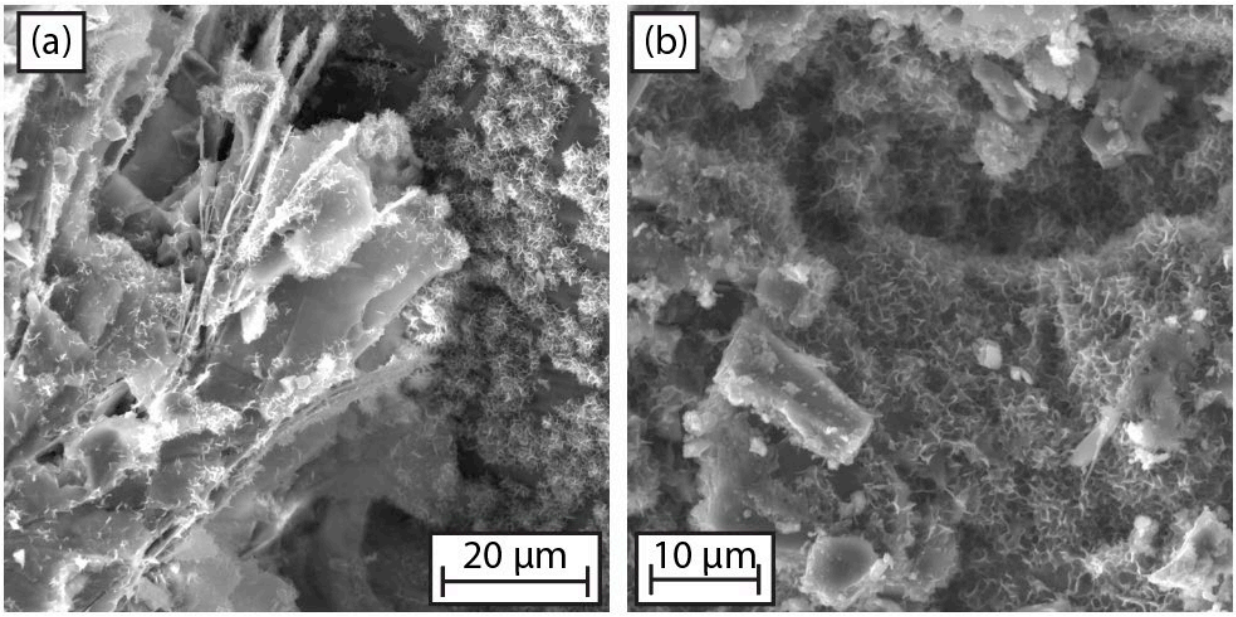

Figure B5. Backscattered electron images of smooth fracture surfaces after experiments conducted at 250 °C under (a) no flow and (b) flow-through conditions.

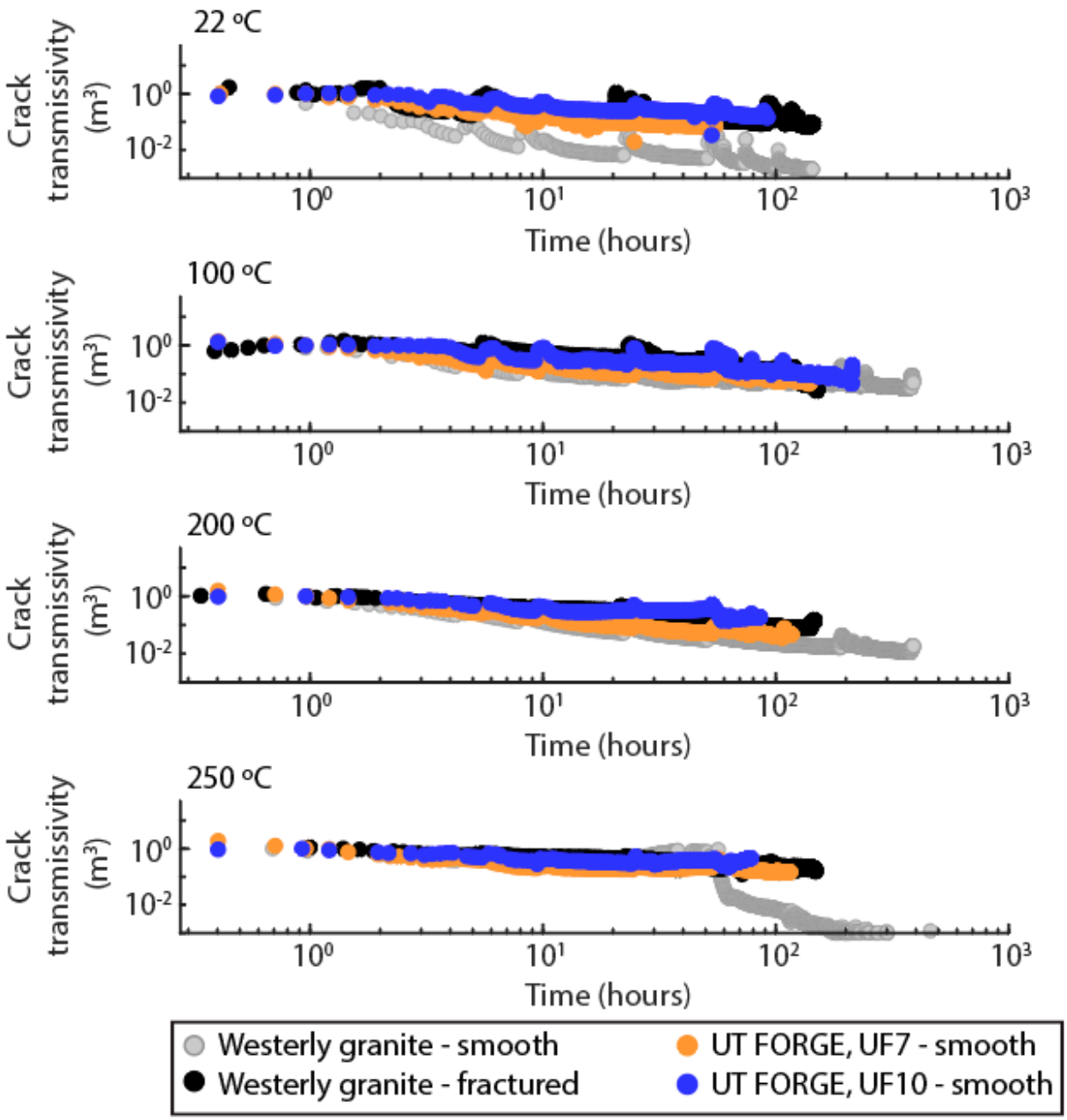

Figure B6. Evolution of crack transmissivity during experiments on smooth and rough fractures at temperatures from 22 to 250 °C. UT FORGE = Utah Frontier Observatory for Research in Geothermal Energy.

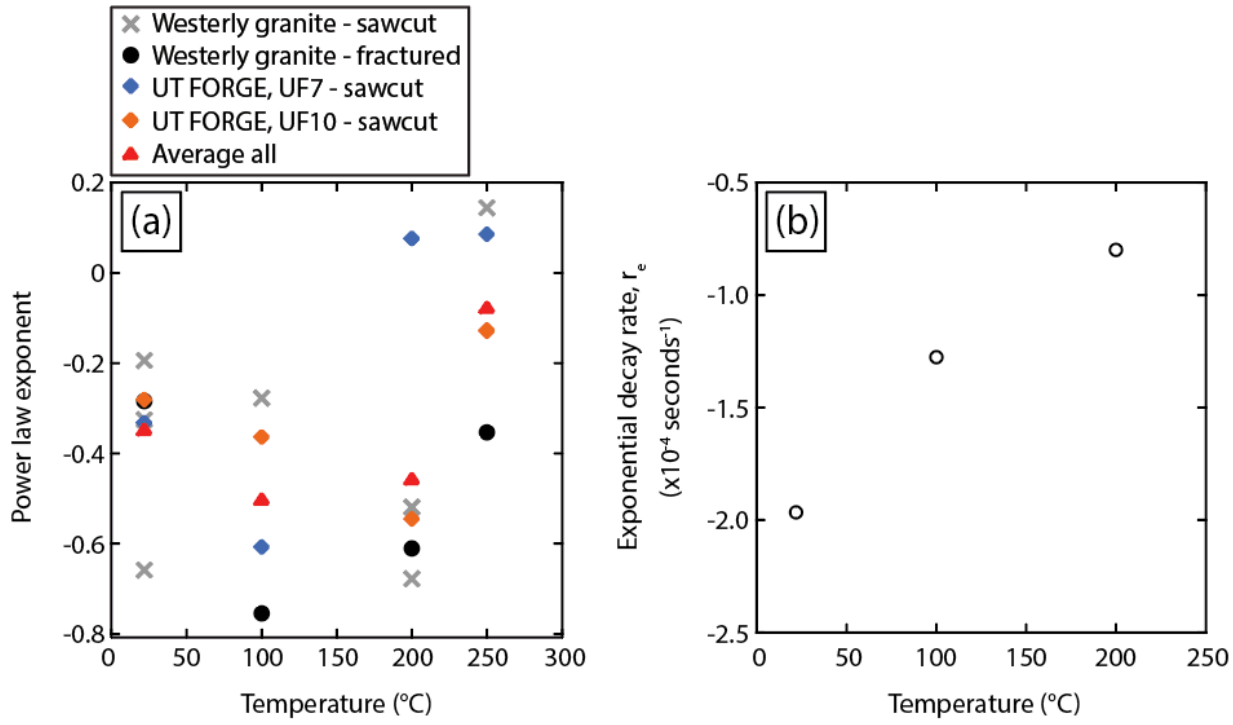

Figure B7. Crack transmissivity decay rates with temperature for (a) the background, long-term behavior and (b) the average short-time-scale decay of shear induced transients. UT FORGE = Utah Frontier Observatory for Research in Geothermal Energy.

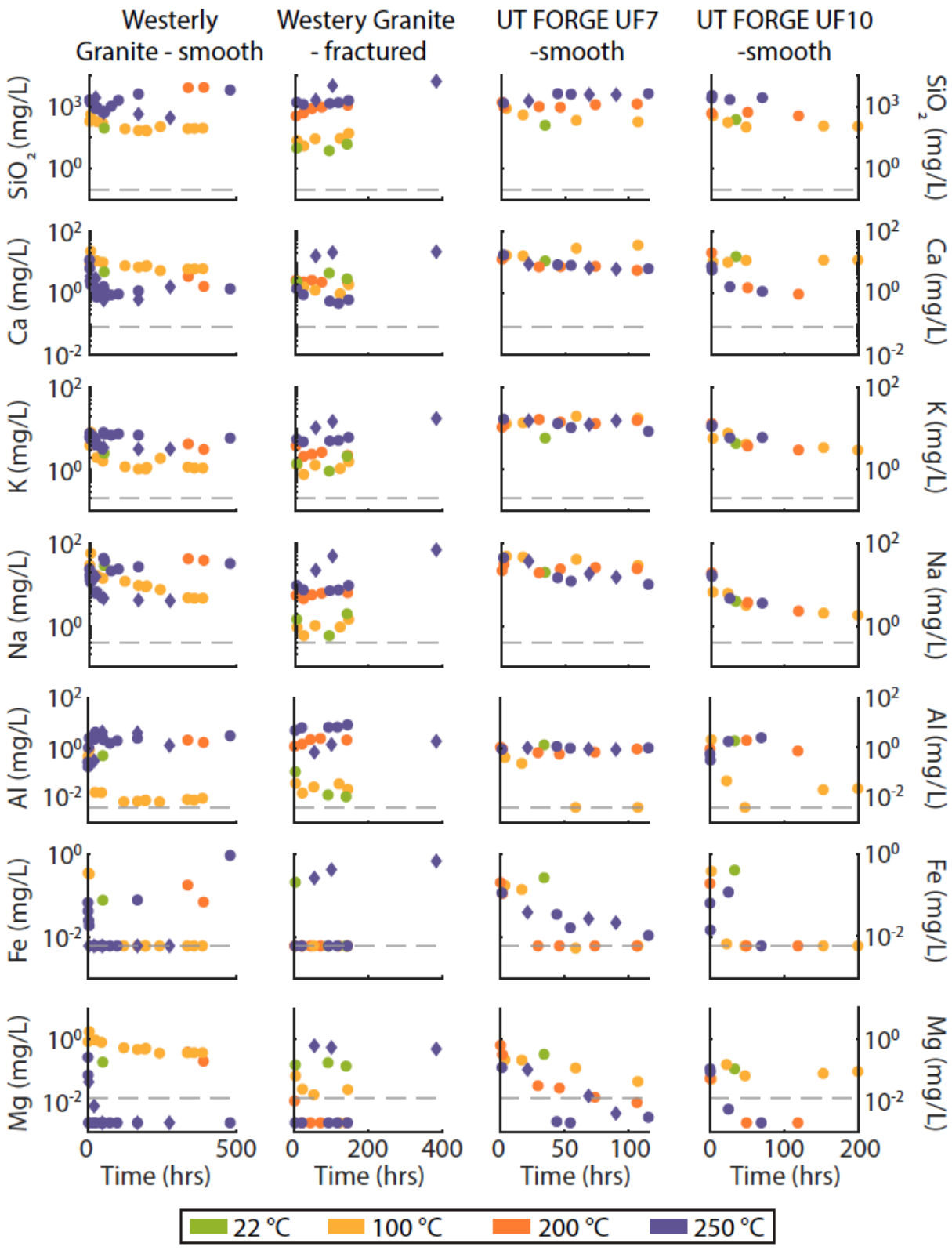

Figure B8. Cation concentrations in pore fluid samples collected periodically during experiments. Gray dashed line reflects the initial composition of the deionized water used as pore fluid. UT FORGE = Utah Frontier Observatory for Research in Geothermal Energy.

C. Supplementary Documents

C1. Single contact experiments

Low contact stress quartz overgrowth experiments

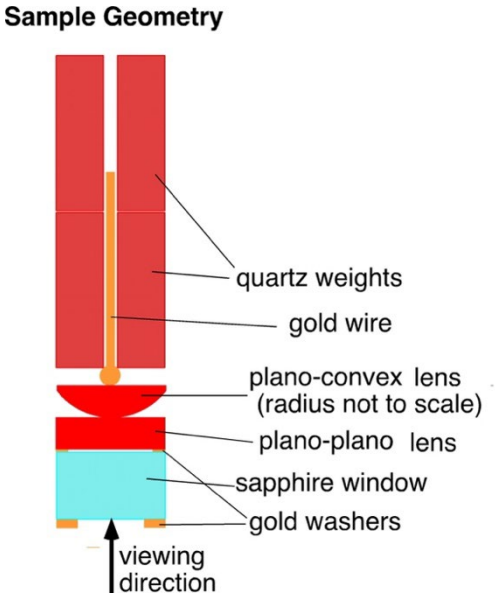

Figure C1. Sample geometry for single contact growth experiments.

We conducted two quartz single contact growth experiments to measure the rate of overgrowth formation at 200 and 300 °C in a hydrothermal vessel with an optical window in the base. The sample geometry is shown at left (Fig. C1). There is a long working-distance microscope focused through the window onto the contact inside the vessel, illuminated by a tunable monochromatic light source. The vessel is completely filled with distilled, de-ionized water at the start of a test, and kept at 75 MPa throughout. Static quartz weights are used to load the contact and ensure that the water in the vessel is maintained at quartz saturation during each run. The contact stress is controlled by the load (0.85 N) and the radius of curvature of the plano-convex sample (~2.4 m). Contact stress is initially approximately 4 MPa. Initial contact radius is about 0.4 mm.

The two-month duration 200 °C experiment did not produce resolvable healing while the 5-month 300 °C experiment did. Overgrowth was visible after two months. An in-situ image of the final contact structure is shown at right (Fig. C2). Reflected monochromatic light produces Newton's rings which measure the aperture of the gap between the lenses; they are contours of gap thickness. There is a well-defined contact margin within the center of the Newton pattern. The image is scaled, and the axes are in mm.

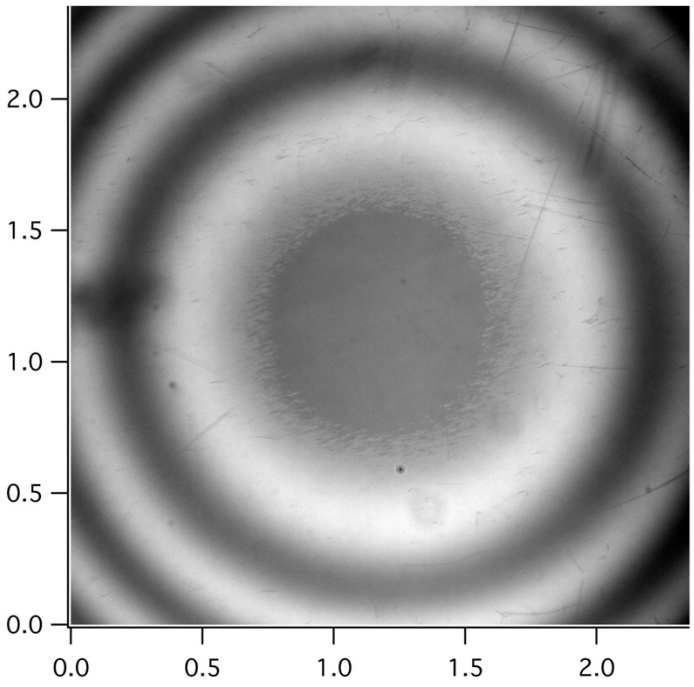

Figure C2. In situ image of the final contact structure for the 5-month 300 °C contact growth experiment

The thermodynamic driving force for contact growth is the high surface curvature at the contact margin. Growth rates are determined from processing scaled images of the contact, taken periodically throughout the experiment. Fig. C3 below shows the inferred growth rate from prior experiments (black symbols, Beeler and Hickman, 2015) between 350 and 530 °C. Contact growth is controlled by the rate of fluid diffusion in these experiments, as evidenced by the aperture dependence of the growth rate and recovered microstructures (see Interpretation below). Dimensional analysis shows the rate resulting from diffusion control is inversely proportional to the aperture squared (Hickman and Evans, 1995; black lines in Fig. C3, refer to figure for key equations). The red dashed-dotted line is the predicted rate based on extrapolating the higher temperature data. The observed rates at 300 °C (red symbols) are much lower and depend more weakly on aperture.

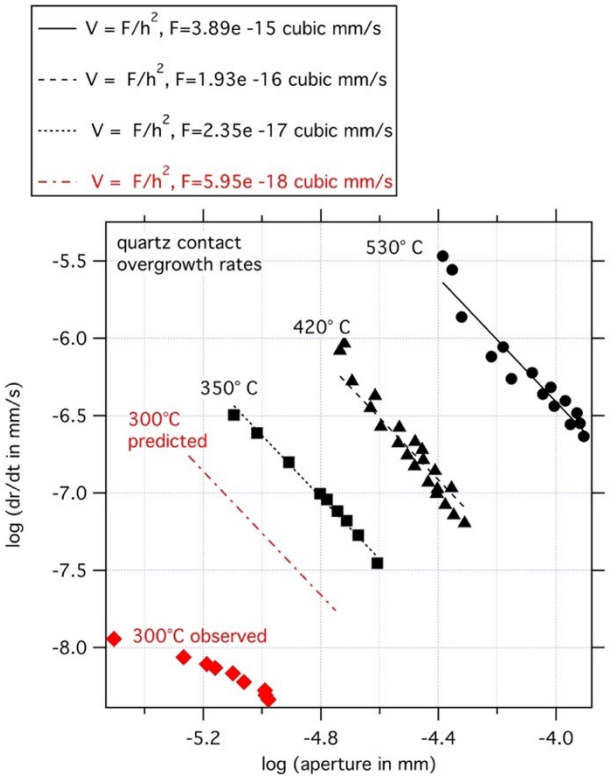

Figure C3. Contact growth rates from Beeler & Hickman (2015; black symbols) and this study (red symbols).

Interpretation and microstructures.

Both the large reduction in contact growth rate and its weaker aperture dependence are expected to accompany a reduction in temperature, if the rate-controlling process switches to precipitation at the contact, rather than diffusion of solute through the pore fluid. Precipitation and diffusion are serial processes, with the overall rate determined by the slower process. Precipitation typically has a higher activation energy and is favored as the rate-limiting mechanism at low temperature (e.g., Rimstidt and Barnes, 1980; Idefonse and Gabis, 1976). Dimensional analysis suggests that the aperture dependence of precipitation rate is inversely proportional to aperture, h^{-1}, as opposed to h^{-2} for diffusion, qualitatively consistent with the observed reduction in aperture dependence in our 300° C experiment.

Conservation of solute volume analysis suggests that diffusion and precipitation-controlled contact growth will produce diagnostic microstructures (Hickman and Evans, 1992). Diffusion will produce prominent dissolution microstructures immediately adjacent to the contact overgrowth (Hickman and Evans, 1992). These arise due to the large curvature gradient in the vicinity of the contact, which locally depletes the solute concentration in solution as material is rapidly precipitated at the contact. As diffusion lags precipitation, the local solution becomes depleted, causing dissolution of the relatively flat surfaces adjacent to the contact. The diagnostic microstructures of diffusion-limited contact growth are near-contact apertures or fluid inclusions within the contact that exceed the initial aperture. Over time these dissolution features become larger, as observed in our 350–530° C experiments. In contrast, precipitation-limited microstructures tend not to produce local dissolution microstructures, as the quartz

concentration in the bulk fluid—both close to and distant from the contact— is buffered to the steady-state concentration required by rapid diffusion of quartz away from the contact.

The microstructures analyzed thus far from the 300° C experiment are from 3D surface profiles of the disaggregated contact. Topography was characterized using a Zygo model 7200 white light interferometer at the University of Oregon CAMCOR facility. In the highest resolution configuration using a 50x objective, the in-plane x, y discretization is 0.22 mm. Generally, the manufacturer's quoted plane-normal z resolution is < 0.05 nm. On the left is a scaled 5x profile of the entire contact having a diameter of approximately 0.8 mm (Fig. C4. The x, y sampling is 2.2 µm. At this scale the microstructure lacks definitive evidence of diffusion control; there are no clear dissolution features adjacent to the outer margin of the contact, in contrast to the formation of peripheral moats as seen in our 350 – 530° C experiments (Beeler and Hickman, 2015). While there are some deep inclusions within the margin of the overgrowth (dark blue), within the contact itself visible inclusions are sub-nm.

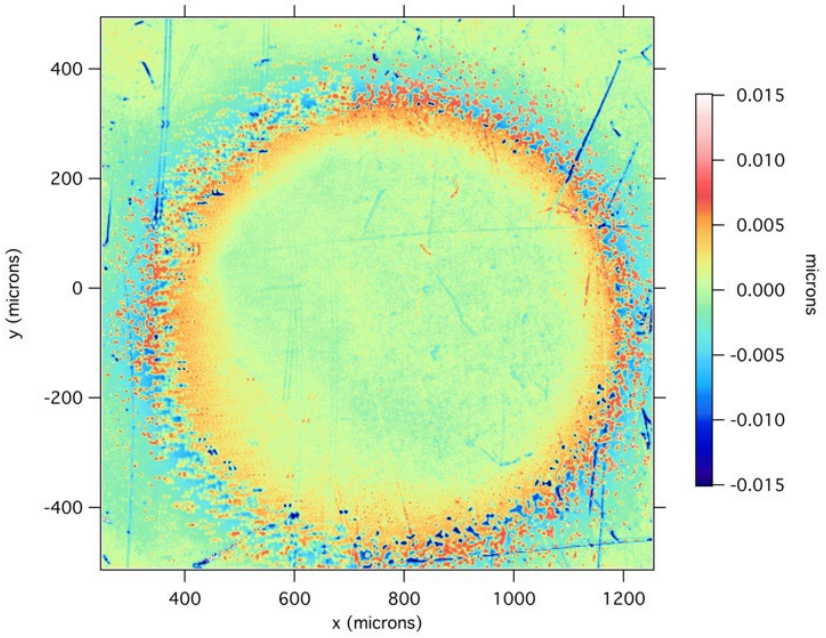

Figure C4. Scaled 5x profile of the entire contact from the 300 °C contact growth experiment.

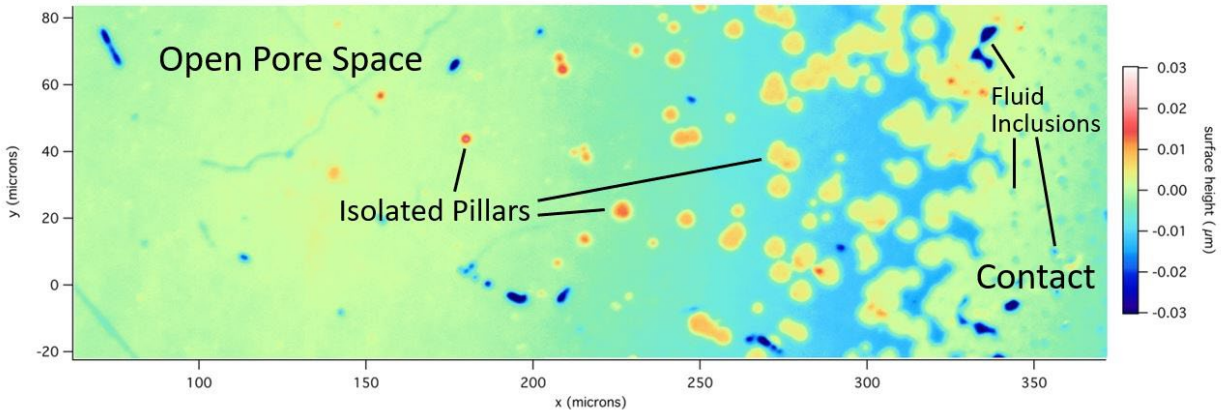

Figure C5. A scaled 50x transverse profile taken from the image of the 300 °C contact growth experiment shown in Fig. C4, starting at ~ 300 µm. Traverse starts from just outside the contact on the left to within the interior of the contact overgrowth on the right.

A 50x traverse (immediately above) from outside the contact on the left side of the image to within the interior of the contact overgrowth on the right (starting at x ~ 300 microns) also lacks strong evidence for diffusion-limited contact growth (Fig. C5). There are no prominent dissolution features at the contact margin and inclusions in the interior of the contact (faint blue dots) have heights of 10 nm or less. Although there are some deeper blue inclusions in the overgrowth having heights of >10 nm, similar amplitude pits are found well outside the growing contact. Overall, these preliminary microstructural observations, while not definitive, are consistent with a transition to precipitation-limited contact growth in our 300 °C experiments.

High stress, pressure dissolution experiments

Analysis of our granite friction experiments suggests that contact scale dissolution or phase transformations may be occurring during slide-hold-slide tests. The mechanical data suggest a strong time-dependent weakening during the hold portion of these tests, consistent either with dissolution or the production of weak material (e.g., clay alteration products) at load bearing contacts. The latter interpretation is most consistent with SEM imaging that shows evidence of alteration of feldspar during these experiments. These observations motivated a second set of single contact experiments, which we recently began and expect to continue past the duration of our Frontier Observatory for Research in Geothermal Energy (FORGE) contract. Unlike the pure quartz overgrowth experiments conducted at low stress, these are high-stress experiments intended to activate stress-enhanced contact dissolution (pressure solution) with or without accompanying mineralogical phase transitions.

The experimental configuration consists of a high curvature quartz single crystal lens (r=0.011 m) in contact with an oligoclase feldspar flat. The design specs are intended to produce an initial contact diameter of ~0.1 mm and a peak contact stress of ~140 MPa. In practice, as shown in the optical interferograms below, the contact in this preliminary experiment is not circular, having a prominent linear feature (a crack, cleavage or twin) that bisects the contact. The image shown in Fig. C6a was acquired in situ at run conditions (300°C, 75 MPa water pressure) at the start of the experiment (12/3/24). After 74 days at run conditions (02/17/25; Fig. 6b); there has been slow growth of the contact. Migration of the interference fringes during this time indicates clear convergence of the upper half contact and some divergence of the lower half contact (i.e., convergence accompanied by rotation about an axis roughly coincident with the linear feature mentioned above). There is no clear evidence of alteration products. At this stage our working hypothesis is that the overall increase in contact area is due to stress-enhanced dissolution within the contact, which may be confirmed by micro-structural analysis. This type of inter-lens convergence was *not* observed in our quartz-on-quartz experiments at the same conditions. If validated by subsequent analyses and observations, this would confirm the effect of dissimilar (polymineralogic) interfaces in enhancing the rates of intergranular pressure solution first observed in the halite-brine system by Hickman and Evans (1991).

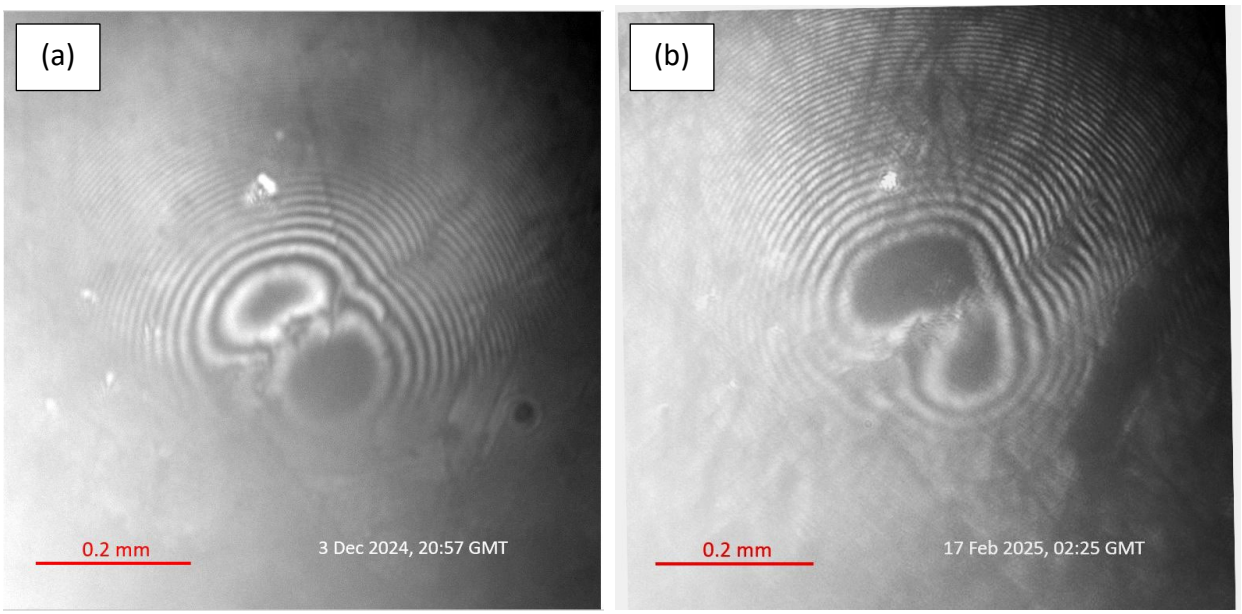

Figure C6. In situ images of the quartz on oligoclase contact structure at (a) the start of the contact growth experiment and (b) after 74 days at 300 °C.

References

Beeler, N. M., and S. H. Hickman (2015), Direct measurement of asperity contact growth in quartz at hydrothermal conditions, J. Geophys. Res. Solid Earth, 120, doi: 10.1002/2014JB011816.

Hickman, S. H., and B. Evans (1992), Growth of grain contacts in halite by solution transfer; Implications for diagenesis, lithification, and strength recovery, In *Fault Mechanics and Transport Properties of Rocks*, ed. B. Evans and T.-f. Wong, pp. 253-280, Academic, San Diego, CA.

Hickman, S., and B. Evans, (1991), Experimental pressure solution in halite, 1: The effect of grain/interphase boundary structure, *Journal of the Geological Society of London*, vol. 148, p. 549-560.

Ildefonse, J.-P., and V. Gabis (1976), Experimental study of silica diffusion during metasomatic reactions in the presence of water at 550°C and 1000 bars, *Geochim Cosmochim Acta, 40,* 297-303.

Rimstidt, J. D., and H. L. Barnes (1980), The kinetics of silica-water reactions, *Geochim. Cosmochim. Acta, 44*, 1683-1699.